

# On the Origin of Strong Magnetic Fields in Young Supernova Remnants

*Byung-Il Jun \*and Michael L. Norman*

Laboratory for Computational Astrophysics  
National Center for Supercomputing Applications  
Department of Astronomy  
University of Illinois at Urbana-Champaign

September 23, 2018

## Abstract

Young supernova remnants such as Tycho generally exhibit a bright circular clumpy shell in both radio and X-ray emission. For several young remnants, various arguments suggest that the magnetic field is larger than can be explained by compression of a few  $\mu G$  ambient magnetic field by the shock wave. Radio polarization studies reveal a net radial orientation of magnetic fields in the shell which cannot be explained by the simple compression either. We model

---

\*Present address : Department of Astronomy, University of Minnesota, 116 Church Street, S.E.,  
Minneapolis, MN 55455, bjun@astro.spa.umn.edu

Rayleigh-Taylor instability at the interface of the ejecta and the shocked ambient medium to explain these observations. We have performed multidimensional MHD simulations of the instability in the shell of a Type-I supernova remnant for the first time utilizing a moving grid technique which allows us to follow the growth of the instability and its effect on the local magnetic field in detail. We find that the evolution of the instability is very sensitive to the deceleration of the ejecta and the evolutionary stage of the remnant. As the reverse shock enters the inner uniform density region, Chevalier’s self-similar stage ends and the thickness of radio shell increases and the instability weakens. Our simulation shows that Rayleigh-Taylor and Kelvin-Helmholtz instabilities amplify ambient magnetic fields locally by as much as a factor of 60 around dense fingers due to stretching, winding, and compression. Globally, the amount of magnetic-field amplification is low and the magnetic energy density reaches only about 0.3% of the turbulent energy density at the end of simulation. Strong magnetic field lines draped around the fingers produce the radial B-vector polarization, whereas thermal bremsstrahlung from the dense fingers themselves produce the clumpy X-ray emission. As a result, the X-ray emission peaks inside of the radio emission. Surface brightness profile shows no detailed correspondence between radio and X-ray emission. Major part of radio and X-ray luminosity comes from the mixing region.

*Subject headings:* Supernova remnants – instability – magnetic fields – MHD simulation

## 1. Introduction

Extensive observations of young supernova remnants (hereafter SNRs) have been made, especially for the prototypical sources Tycho, Kepler, and Cas A. These

SNRs are believed to belong to the pre-Sedov stage characterized by a shock expansion law that is faster than the  $t^{2/5}$  law expected for Sedov expansion (Tan and Gull 1985), and a two-shock structure (Ardavan 1973; McKee 1974). These SNRs generally show a circular, clumpy shell near the outer boundary of the remnant in the radio and X-ray emissions. The magnetic field strength in the radio shell has been inferred to be in the range of  $10^{-4} \sim 10^{-3}G$  by assuming equipartition of energy between magnetic fields and relativistic particles (Strom and Duin 1973; Henbest 1980; Anderson et al 1991). Other arguments suggest that the low limit of the magnetic field in young SNRs is much larger than the compressed value of ambient magnetic field obtained by simple shock compression (Cowsik and Sarkar 1980; Matsui et al. 1984; Reynolds and Ellison 1992). The locations of the inner radio shell and the clumpy X-ray emission in Tycho's SNR coincide although there is no detailed correspondence between radio and X-ray features (Dickel et al. 1991). Detailed radio polarization studies reveal that the magnetic field in the shell exhibits a cellular pattern with a net radial orientation (Downs and Thompson 1972; Milne 1987; Dickel et al. 1991). In addition to these generic features of young SNR, a thin bright rim (sharp outer boundary) in radio emission exist in Tycho's SNR (Dickel et al 1991) and the SNR of A.D. 1006 (Reynolds and Gilmore 1986,1993). The rim in Tycho's SNR has a typical degree of polarization of 20% to 30% while the degree of polarization within a cell in the main shell is about 7% (Dickel et al 1991). Tycho's SNR and the SNR of A.D. 1006 show the coincidence of sharp edges in radio and X-ray emission which is generally interpreted as the locus of the shock front. They are presumed to have been Type I events implying that the remnant expanded into a medium of roughly constant density. Our study is motivated to understand the

origin of these generic features of young remnants of Type I supernova by means of numerical simulation.

It has been suggested that the contact interface between the ejecta and the shocked ambient medium is Rayleigh-Taylor (hereafter R-T) unstable (Gull 1973) due to the strong deceleration felt by the denser ejecta as it sweeps up lighter ambient gas. The R-T instability in the decelerating stage (pre-Sedov stage) has been studied in one space dimension by Gull (1973,1975) and Dickel et al. (1989). Chevalier et al. (1992) extended the study of the instabilities to two dimensions by modeling the interaction region assuming self-similar flows and without the inclusion of a magnetic field. They found that a turbulent mixing layer is produced in the nonlinear state. Such mixing could amplify the interstellar magnetic field to the inferred milligauss values, and thus the incorporation of magnetic fields into multidimensional simulations is of great importance. Here, we present the first study of the evolution of the R-T instability in young remnants of Type I supernova by two-dimensional MHD simulations. Since we simulate the entire remnant, our calculation is not restricted to the self-similar stage, and thus we are able to study the growth and eventual saturation of the instabilities for the evolving remnant. As a consequence, we are able to predict the evolution of the integrated X-ray and radio luminosity of the remnant during the first 500 years. Subsequent papers will extend this study to 3D MHD (Jun and Norman 1995b) and greater dynamical ages (Jun and Norman 1995c).

The linear theory of the classical R-T instability has been fully studied by Chandrasekhar (1961). The nonlinear growth of the instability has been studied numerically (Sharp 1984; Youngs 1984,1991). In a previous work, we have explored the clas-

sical R-T instability in incompressible magnetic fluids by two- and three-dimensional MHD simulations (Jun, Norman, and Stone 1995, hereafter JNS). Although highly idealized, these simulations support Gull’s picture that the radial magnetic field in the main shell of SNR can be produced as the R-T fingers stretch existing field lines. The present simulations put Gull’s hypothesis to the test in a realistic astrophysical context. We find that Gull’s model is able to explain a clumpy bright radio shell which is generated by the turbulent amplification of magnetic fields through the R-T instability. Our simulation is also able to explain radial magnetic fields in the main shell. The evolution of the instability and the radio shell is a sensitive function of the deceleration of the ejecta and the evolutionary stage of the remnants.

In this paper, we present the results of MHD simulations of the instabilities in young SNRs in a uniform ambient medium and attempt to explain some of observational features of Type I SNR. Section 2 presents the initial conditions and numerical method. Results are presented in Section 3, and a discussion of our numerical limitations is given in Section 4. We then compare our model with observations and conclude in Section 5.

## 2. Initial condition and numerical method

We initialize the outer 3/7 of the star of mass  $1.4 M_{\odot}$  with a power law density profile  $\rho \sim r^{-7}$  and the inner 4/7 of the star with a constant density to mimic Type-Ia supernova remnants (Colgate and McKee 1969). An explosion of energy of  $10^{51} \text{ ergs}$  is deposited as kinetic energy where the velocity is assumed to be linearly

proportional to the radius. The radius of the inner core ( $r_c$ ), the density of the inner core ( $\rho_c$ ), and the velocity at the outer boundary of the ejecta ( $v_0$ ) are now given by,

$$r_c = R \left( 1 - \frac{x(3-n)M}{4\pi\rho_0 R^3} \right)^{\frac{1}{3-n}}, \quad (1)$$

$$\rho_c = \frac{3(1-x)M}{4\pi r_c^3}, \quad (2)$$

$$v_0 = E_k^{1/2} \left( \frac{2\pi\rho_c r_c^5}{5R^2} + \frac{2\pi\rho_0 R^3 (1 - (R/r_c)^{n-5})}{5-n} \right)^{-1/2} \quad (3)$$

where  $R$  is the radius of the ejecta,  $x$  is the mass fraction of the outer power law density region which is  $3/7$  in our case,  $n$  is the density power index of the outer region,  $M$  is the total mass of the ejecta,  $\rho_0$  is the density of ejecta at  $R$ , and  $E_k$  is the total kinetic energy. The background density is chosen to be uniform with  $1.67 \times 10^{-24} g/c.c.$ . The temperature of the entire region is taken as  $10^4 K$ . The background magnetic field is chosen to be  $3.5 \mu G$  and assumed to be tangential to the shock front and lying in the simulation plane. A second simulation assumed a toroidal magnetic field which is perpendicular to the two-dimensional plane. We will focus our study on the case with an initial pure poloidal field since the amplification of the magnetic field occurs by the stretching of the poloidal field line. The density is initially perturbed within the entire region of computational space with a random noise of 2.0% amplitude. We start the simulation at  $R = 0.1 pc$ . Although this value is larger than the stellar radius of the presupernova, the important variable in the evolution is mass ratio rather than the initial radius. The mass ratio  $\mu$  is defined by the swept-up mass by the forward shock divided by the ejected mass. This mass ratio represents the dynamical age of the remnant because the velocity of the remnant is determined by the mass ratio from momentum conservation argument. Therefore,

the mass ratio is a meaningful quantity for the age rather than time.

We solve the ideal compressible MHD equations in a moving Eulerian grid using the ZEUS-3D code originally written by David Clarke and further developed by the Laboratory for Computational Astrophysics at the University of Illinois, Urbana-Champaign. Shocks are stabilized by von Neumann-Richtmyer artificial viscosity. Magnetic fields are transported using Constrained Transport (Evans & Hawley 1988) modified with the Method of Characteristics (Stone & Norman 1992b) to satisfy the divergence-free constraint and to treat Alfvén wave properly. The code includes no physical diffusion term, and the numerical diffusion is determined by the grid resolution. Readers are referred to Stone & Norman (1992 a,b) for the detailed description of algorithms of the code.

A moving grid method is used to maintain high resolution in the region between the forward shock and the reverse shock. Basically, the velocity of the forward shock is measured numerically every time step and it is assigned to the grid velocity at the shock front. All other grids are also expanding homologously at every timestep. A large number of zones are distributed uniformly between the outer and reverse shocks. The region inside the reverse shock is resolved with ratioed zones which increase in size as  $r \rightarrow 0$  in order to avoid a too stringent Courant condition on the timestep (Fig.1). This method allows us to keep the high resolution at the intershock region and to avoid a very small timestep near the origin. We used a wedge of  $\pi/4$  in spherical polar geometry, and periodic boundary conditions at the angular boundaries and reflecting boundary condition at the origin. The intershock region is resolved with  $200 \times 400$  grids and the region inside the reverse shock is

resolved with  $100 \times 400$  grids.

To track the contact discontinuity between the ejecta and the ambient material, we evolve the mass fraction continuity equation (see JNS) :

$$\frac{\partial(m_f \rho)}{\partial t} + \frac{\partial(m_f \rho v_i)}{\partial x_i} = 0 \quad (4)$$

where  $m_f$  is the mass fraction of the ejecta. The initial mass fraction distribution is 1 for the ejecta and 0 for the ambient medium. This method is particularly useful in the study of the mixing layer.

### 3. Results

#### 3.1. 1D results

We first carried out the simulation in one dimension to an age of 500 years to study the evolution of the remnant without the instability. At this time, the mass ratio is 3.94. The basic physical variables at 100 years ( $\mu = 0.23$ ) are shown in Fig.2. It can be seen from the distribution of grid points that our moving grid technique follows the forward shock accurately. The intershock region agrees well with Chevalier's self-similar solution (1982). The magnetic field profile agrees well with the simulation of Dickel et al.(1989). The magnetic field is the strongest at the contact discontinuity at this time. Nonetheless, the magnetic field is essentially passive. This can be seen by comparing the magnetic energy density  $\frac{B^2}{8\pi} \approx 10^{-11} \text{erg/cm}^3$  to the kinetic energy density  $\frac{1}{2}\rho v^2 \approx 10^{-6} \text{erg/cm}^3$ . By 300 years the reverse shock has reached the inner region of the constant density (Fig.3), and the intershock region has broadened. As



a result, the density at the reverse shock and magnetic field strength at the contact discontinuity decrease accordingly (see also Fig.4). The mass ratio at 300 years is about 1.6. According to Chevalier (1982), the self-similar solution is valid for  $t < t_c$  where

$$t_c = 0.36 \left( \frac{M^5}{E_k^3 \rho_a^2} \right)^{1/6} \quad (5)$$

and  $\rho_a$  is the ambient density. For our parameters,  $t_c = 225yr$ . Our simulation agrees well with this value. Fig.5 shows the comparison of evolutions between the self-similar solutions for  $n=7$  and  $s=0$  (Chevalier 1982) and our numerical solutions at the contact discontinuity. The numerical solution shows a higher velocity than predicted by the self-similar solution until 345 years, thereafter becoming slower. As explained by Band and Liang (1988), this slowdown occurs because when the reverse shock moves into the inner core of the ejecta, the density upstream of the reverse shock decreases, and the force of the “piston” weakens. Note the deceleration of the ejecta is the strongest at the earliest stage. This strong deceleration directly affects to the evolution of the instability as we will see in the 2D simulation.

## 3.2. 2D results

### 3.2.1. Evolution of the instabilities

The generalized condition for R-T instabilities can be written as (Jones et al. 1981)

$$\frac{\partial \ln \rho}{\partial x} \frac{\partial P}{\partial x} < 0 \quad (6)$$

Basically, this condition states that the local density gradient  $\frac{\partial \rho}{\partial x}$ , is in the opposite direction of the local effective gravity  $g$ , where for local hydrostatic equilibrium  $g = \frac{1}{\rho} \frac{\partial P}{\partial x}$ . If this condition is satisfied, denser fluid is sitting atop lighter fluid in an effective gravitational field, and this is unstable. The region near the contact discontinuity is most unstable (Fig.2) by this criterion. At early times, the short wavelengths appear first because the growth rate is inversely proportional to the square root of the wavelength. Large fingers become dominant at later stages because larger fingers feel less drag and reach a higher terminal velocity than smaller fingers. The terminal velocity is proportional to  $\sqrt{gr}$  where  $r$  is the radius of the finger. As the finger grows, it streams ahead of the shocked ambient gas, and thus the boundary of the finger becomes sheared. As a consequence, the Kelvin-Helmholtz (hereafter K-H) shear wave instability develops and mushroom caps, which are regions of high vorticity, are generated at the tips of the fingers. K-H instabilities on the side of the finger can even detach the finger. Because of flux freezing, the magnetic fields are amplified by shearing and stretching at the finger boundaries (on the other hand, in the case with an initial toroidal magnetic field, interchange modes develop and no amplification of the magnetic fields occurs because there is no stretching of the field lines.). Fig.6 shows the grey scale images of density (left) and magnetic pressure (right) in the shell region at 100,200,300,400,and 500 years from bottom to top. The wider intershock region is noticeable at 400 and 500 years. The wavelength of instability increases as the intershock region becomes wider. The thickness of the mixing layer is about half of the magnetic shell thickness at 500 years where the magnetic shell is defined as the region between the outer shock and the innermost boundary of R-T bubbles. Our results show well developed mushroom caps at

the tips of fingers due to the K-H instability in good agreement with the purely hydrodynamic simulations of Chevalier et al. (1992). Both the forward shock and reverse shock are clearly seen and are not significantly influenced by the instabilities. Notice that the reverse shock is not seen in the image of magnetic pressure because the mixing due to the instability does not reach to the reverse shock.

The effects of compressibility on the evolution of the fingers is significant. As fingers approach the forward shock, they move into a higher pressure environment and are compressed. For instance, the density at the reverse shock in 1D was about  $4.6 \times 10^{-24} g/cm^3$  at 500 years. In the 2D simulation, a higher density of  $5.5 \times 10^{-24} g/cm^3$  is found near the tip of some fingers as an evidence of the compression. As a result, magnetic fields are amplified by compression as well as stretching. The strongest magnetic fields are seen along the sides and tips of the fingers rather than at their base where bubbles of shocked ambient medium collect. This is because in the fluid frame the fingers have a higher speed than the bubbles. A detailed image at 500 years is shown in Fig.7. It shows, from top to bottom, grey scale images of the density, the magnitude of magnetic field, the vorticity, and the current density. It is clearly seen that the vorticity in the wings of mushroom cap is the strongest. However the magnetic field is not strong in the strong vorticity region. One might naively expect that the magnetic field should be strong in that region as well since the vorticity and the magnetic field obey the same equations in an incompressible fluid with a passive field. This is not the case in our 2D calculation because magnetic field and vorticity have very different initial values, the vorticity has only a component in the perpendicular direction to the simulation plane, while there is no B-field in this direction. The current density is found to be strong where mushrooms collide with

each other. Current sheets form and magnetic reconnection can occur. Cattaneo et al.(1990) in a study of bouyancy-driven instabilities, also found that magnetic reconnection occurs when mushrooms detach themselves from the layer and when they collide with each other.

The instability is strongest at about 60 years as we can see in Fig.8. The turbulent energy density is defined as peculiar kinetic energy density by excluding the contribution from pure expansion of the SNR,  $E_{tur} = \frac{\int \frac{1}{2}\rho(v_{1,p}^2+v_{2,p}^2)dV}{\int dV}$  where  $v_{1,p}$  and  $v_{2,p}$  are defined as  $v_1 - \bar{v}_1$  and  $v_2 - \bar{v}_2$ , and  $\bar{v}_1$  and  $\bar{v}_2$  are the angular average of  $v_1$  and  $v_2$ , respectively. The strong deceleration at the early stage drives the rapid increase of the turbulent energy. After the first peak, the turbulent energy density decreases rapidly due to the weak deceleration, and then it tends to stay for a while during the self-similar stage (saturation of the instability). At around 300 years, the turbulent energy density starts to decrease again because the remnant evolves beyond the self-similar stage. Now the reverse shock enters the constant density region of an inner core, the intershock region becomes wide, and the instability weakens. About 5.8% of initial kinetic energy transfered into the turbulent energy by the end of simulation.

The evolution of the magnetic energy density reflects the evolution of the instabilities directly since the magnetic field is amplified by the turbulent flows. The magnetic energy density is defined as peculiar magnetic energy density which exclude the initial magnetic field and shocked magnetic field. So, the peculiar magnetic energy density contains the magnetic field amplified by the instabilities only. The total magnetic energy density decreases from about 380 years due to the weakened insta-

bilities and the decreased strength of magnetic fields near the contact discontinuity (see figures 3 and 4). The evolution of the thickness of a magnetic shell and the thickness of an intershock region is shown in Fig.9. The self-similar stage which can be noticed from the constant thickness persists until about 220 years. The big bump of magnetic shell up to 100 years represents the vigorous instability due to the strong deceleration at early stage. The image at 100 years in Figure 6 reveals some of bubbles penetrating close to the reverse shock front which result in a thicker magnetic shell.

### 3.2.2. Strength and Distribution of Magnetic Fields

Initially, the magnetic field is effectively passive as the supernova energy exceeds the swept up magnetic energy by many orders of magnitude. We now ask whether the field becomes dynamically important as it is amplified. To answer this question, we compute the energy spectra. From Fig.10, we can see that the turbulent energy density exceeds the magnetic energy density at all scales. Therefore, we can say that the magnetic field has not reached the equipartition globally on any scale contrary to the usual assumption. In Fig.8 it is also seen that the turbulent energy density is greater by about factor of 300 than the magnetic energy density. The magnetic energy achieved by the instability is about 0.3% of the turbulent energy at the end of simulation. Even though the field has not reached equipartition globally, it may be dynamically important locally. To investigate this, we compare the turbulent energy density and magnetic energy density at each cell. We find that the field

becomes dynamically important at the tips of some fingers and around the fingers although the region with dynamically important field is only a very small fraction of the magnetic shell. This fraction is likely to increase with the numerical resolution. We discuss this issue further in section 4.

The angular averages of total magnetic field at 500 years are compared to the result of 1D simulation in Fig.11. The 2D result shows the peak magnetic field strength is near the contact discontinuity due to the amplification by the R-T instabilities. We can see the generation of radial component of the magnetic fields quite clearly in the third plot, as well as the amplification of the tangential magnetic field in the fourth plot. In Fig.8, it is found that the radial component of peculiar magnetic energy density is comparable to circumferential(tangential) component. At 500 years, the radial field becomes the dominant component with an energy density of about 1.4 times the circumferential component (Fig.8) when we consider only the peculiar magnetic energy which is the result of the instability. It seems that the relative magnetic energy density of the radial component increases as the mixing region becomes wider allowing the formation of longer fingers.

Fig.12 shows the spectra of peculiar magnetic energy components at 400 years and 500 years. The radial field is dominant in the large scale structure (mode number, 13 to 18) although the relative strength fluctuates depending on the size of the structures. It seems that the dominance of radial field in the large scale in our simulation may be able to explain the net radial orientation of the magnetic field in young supernova remnants if the magnetic field in the ambient medium is disordered unlike the initial condition of our simulation. It should be noted that the direct quantity to

look at is not the magnetic energy but the radio polarization because the magnetic energy component is not necessarily proportional to the polarization. Since our simulation is restricted to two-dimensional space, we are unable to address the radio polarization directly. A future paper will report on fully 3D MHD simulations of the Rayleigh-Taylor instability in SNR (Jun 1995; Jun and Norman 1995). Polarization mapping of our 3D model confirms that peculiar B vectors in the main radio shell are highly polarized in radial direction. At the moment, our 2D simulations only illustrate the main mechanism responsible for producing radial magnetic fields in young SNR.

### 3.2.3. Radio and X-ray emission

To extract some observational features from our simulations, we have computed the radio and X-ray emissivity. We assume that X-ray emission comes from thermal bremsstrahlung while radio emission is due to nonthermal synchrotron radiation. For X-ray, we take the total amount of energy radiated in free-free transitions per  $cm^3$  per *second* integrated over all frequency (Spitzer 1978)

$$\epsilon_{ff} = 1.426 \times 10^{-27} Z_i^2 n_e n_i T^{1/2} \langle g_{ff} \rangle \text{ ergscm}^{-3} \text{ s}^{-1} \quad (7)$$

where  $Z_i$  is the atomic number of ion  $i$ ,  $n_e$  is the electron density,  $n_i$  is the ionic density,  $T$  is the gas temperature, and  $\langle g_{ff} \rangle$  is the mean Gaunt factor. The mean atomic number (19.4) of ion in the ejecta is obtained from the modeling of Tycho's SNR by Hamilton, Sarazin, & Szymkowiak (1986). Heavy element abundance is

assumed to be constant in the ejecta material. The weighted average between the ejecta and ambient material is computed for the abundance in the mixing region by using the mass fraction distribution. In actuality, the detailed X-ray emissivity is more complicated due to the line emission of heavy elements, nonequilibrium ionization effects, and so on. For example, it is shown that nonequilibrium effects enhance X-ray emission from young SNR (Shull 1982). Our choice of thermal bremsstrahlung for X-ray emission should be applicable only to energies above 2 keV.

The nonthermal radio emissivity (synchrotron emission) is written as (Clarke 1988)

$$i(\nu) \propto \rho^{1-2\alpha} p^{2\alpha} (B \sin\psi)^{\alpha+1} \nu^{-\alpha} \quad (8)$$

where  $p$  is the gas pressure,  $B$  is the magnetic field strength,  $\psi$  is the angle between the local  $B$  field and the line-of-sight,  $\nu$  is the frequency of radiation, and  $\alpha$  is the spectral index and taken as 0.6. This formula is derived by assuming that the population density of the relativistic electrons have a power law spectrum. Since we are not modeling the acceleration and transport of relativistic electron, it is assumed that the number of relativistic electrons is proportional to the gas density and the electron acceleration efficiency does not change with time. This assumption requires that electron diffusion lengths are short enough to confine relativistic electrons to the same fluid element. One should note that this assumption could also be violated under the adiabatic expansion since the relativistic gas has an adiabatic index of 4/3. We postpone a better modeling of radio emission including the acceleration of electrons by the shock wave to a future project. Meanwhile, our model implies that the radio emissivity is a strong function of magnetic field and weak function of gas density. The exact proportionality constant depends on the fraction of relativistic



electrons in the bulk fluid, which is unknown.

The X-ray and radio emissivities at 500 years are shown in Fig.13. The left image is radio emissivity and the right image is X-ray emissivity. Generally, the radio emission is strongest around the R-T fingers because the magnetic field is most strongly amplified there by stretching and winding. On the other hand, the radio emission is rather faint near the R-T bubbles. Note that the reverse shock is not seen in the radio image because of the absence of magnetic field while it is seen in the X-ray image. However if the magnetic fields in ejecta is not negligible as Lou (1994) suggested, the reverse shock should be seen in radio observations. The strong X-ray emission from the R-T fingers are noticeable, which is due to the high abundance of heavy element in the ejecta material. Fig.14 shows the surface brightness in radio and X-ray computed by integrating the emissivity along rays. In our 2D simulation, we ignore  $\psi$  for the moment. The realistic emission map by considering viewing angle and local  $\psi$  can be produced in 3D simulation (Jun and Norman 1995). Each plot corresponds to the surface brightness at 100, 200, 300, 400, and 500 years from top to bottom. The radius is normalized by the radius of the outer shock and brightness is normalized by the maximum brightness. The bright shell exists inside of the outer shock in both radio and X-ray. The radio emission shows more fluctuation in the structure than X-ray. The surface brightness at the outer shock is very weak due to the limb darkening effect. Radio surface brightness peaks near the contact interface while X-ray surface brightness peaks near the reverse shock but they are close to each other. As the remnant ages, the peak X-ray surface brightness near the reverse shock decreases relative to the brightness at the forward shock as the density decreases. The main X-ray shell becomes broader as the remnants gets

older due to the broader mixing layer in the non-self-similar stage. Therefore, the thickness of the X-ray shell is an indicator for the remnant's age.

Fig.15(a) shows the evolution of radio luminosity. Radio luminosity is computed by integrating radio emissivity (see equation 8) over the volume considering  $\phi$ -symmetry, that is  $L_{radio} = \int \int \int i(\nu)r^2 \sin\theta dr d\theta d\phi = 2\pi \int \int i(\nu)r^2 \sin\theta dr d\theta$ . Although this quantity is not exactly the true radio luminosity because we ignored the  $\psi$  dependence in the emissivity, it is still closer to the observed radio luminosity than the integration of emissivity over the computational plane. The dotted line represents the luminosity from the main shell where the instability occurs. This is chosen to be the region up to  $r_{shell} = 0.91r_{shock}$  where the R-T fingers reach the farthest. The dashed lines represent the luminosity from the region between  $r = r_{shell}$  and  $r = r_{shock}$ . The total radio luminosity increases until about 375 years ( $\mu = 2.4$ ) and then it starts to decrease. The radio luminosity from the instability shell region (main shell) always dominates over the radio luminosity from the forward shock region. The decrease of radio luminosity from the main shell at late times is attributed to the weakened magnetic field strength (1D effect) near the contact discontinuity (see Fig.3) and the weakened instability (2D effect) after the remnant leaves the self-similar stage. The radio luminosity from the forward shock region stops increasing at about 300 years due to the decreased pressure behind the forward shock (cf. equation(8)). The evolution of X-ray luminosity which is only applicable to energies above 2keV is shown in Fig.15(b). X-ray luminosity is also computed by integrating X-ray emissivity over the volume, that is  $L_{X-ray} = 2\pi \int \int \epsilon_{ff}r^2 \sin\theta dr d\theta$ . A peak of X-ray luminosity appears earlier than that of radio luminosity because the X-ray emission is sensitive to the density decrease near the reverse shock after the

self-similar stage. The X-ray luminosity is dominated by the main shell due to the heavy elements in the ejecta material. Our model predicts that the time history of each luminosity component is another indicator of the remnant’s dynamical age. The decline of the radio luminosity at late times is also seen by Dickel et al. (1993) in their modeling of clumpy circumstellar medium. They explain that the decline is due to the result of the different shock expansion rates which result from different encounters by the shock with shell clouds. In our uniform ambient medium R-T model, it is due to the decreased mixing which occurs beyond the self-similar stage.

Because we are concerned about our ability to reliably model the physics of the mixing layer (see discussion on “numerical limitation”) which, as we have shown, dominates the radio and X-ray emission at early times, we ask what fraction of the radio emission comes from the strongest amplified fields. Fig.16 shows the radio luminosity distribution as a function of magnetic field strength at  $t=400$  years. The top histogram shows the luminosity distribution emitted from the whole remnant and the bottom one shows only the contribution from the peculiar magnetic fields which is computed by subtracting magnetic fields from the angular averaged magnetic fields. These peculiar components of magnetic fields results from the instability. About 55 % of total luminosity comes from the range between  $B = 9.2 \times 10^{-6}G$  and  $B = 1.45 \times 10^{-5}G$  in the simulation with resolution 300x400. The maximum strength of magnetic field is  $2.1 \times 10^{-4}G$  at this time. Therefore the bulk of the radio luminosity comes from relatively weak fields. The contribution of peculiar components of magnetic fields to the radio luminosity is about 42 %. On the other hand, about 58% of the total luminosity is within the range between  $B = 9.2 \times 10^{-6}G$  and  $B = 1.45 \times 10^{-5}G$  in the simulation with resolution 180x200. And the contribution

from peculiar magnetic fields is about 38% of the total luminosity in this resolution. This result shows a tendency in which the higher resolution simulation produces a greater proportion of the radio luminosity due to the instability than the lower resolution simulation. The bottom histograms show the luminosity distributions from the peculiar magnetic fields for two different resolutions. In general, the magnetic fields due to the instability (peculiar component) is stronger than the simple shocked fields. Increasing the resolution tends to move the luminosity distribution to the stronger magnetic fields. Whether strong magnetic fields (here a strong magnetic field means the field stronger than the shocked magnetic field.) will dominate over total luminosity as the resolution increases further is unclear. It will depend on not only the efficiency of magnetic field amplification but also the volume of the mixing layer over the whole radio shell.

#### 4. Numerical Limitations

Our goal is to construct realistic models of Type-I SNR. In this work we have explored for the first time multidimensional nonlinear effects which strongly influence the radio and X-ray properties of young SNR. Nonetheless, our current simulation has several numerical limitations which require further improvement for the better understanding of SNR, which we now discuss. First, our simulation is restricted to two dimensional space. As studied by JNS, 3D simulation of the classical R-T instability generally produces a somewhat broader mixing layer (about 40 % broader than 2D) due to greater finger penetration in 3D than in 2D. If the R-T bubbles

reach the reverse shock in 3D, they may distort its shape. Generally, mixing in 3D simulations is quite different due to the additional degree of freedom (see JNS). We also expect that 3D simulations may produce a more dominant radial field than 2D. In addition, 3D simulations may produce stronger magnetic fields just as we found in the study of the classical MHD R-T instability (JNS). Stronger magnetic fields in 3D will result in a higher surface brightness as an observational consequence. 3D simulations analogous to the ones presented here have been recently carried out by us, and we will report on them in a subsequent paper. Second, we have not included any physical resistivity since we solved the ideal MHD equations. The magnetic Reynolds number is a function of the magnetic diffusivity and its magnitude influences the amplification of magnetic fields. In addition, the magnetic Reynolds number determines the speed of magnetic reconnection. In our ideal calculation, the grid resolution sets a numerical magnetic Reynolds number which increases as the inverse of the cell size to some power  $\geq 1$ , which in turn is set by the order of accuracy of the algorithm.

To diagnose the numerical difficulty in studying the turbulent amplification of magnetic fields in real SNR, we estimate the numerical magnetic Reynolds number in our simulation by using the relation between the magnetic fluctuations and the magnetic Reynolds number (Vainstein & Rosner 1991) :

$$\langle B^2 \rangle \approx R_M \langle \vec{B} \rangle^2 \quad (9)$$

where  $R_M$  is the magnetic Reynolds number. This relation is valid for passive magnetic fields, which is close to our case. By comparing the relative magnitudes of  $\langle B^2 \rangle$  and  $\langle \vec{B} \rangle^2$  in the mixing layer of our simulation, we derive  $R_M \approx 50$ .

This number is many orders of magnitude smaller than in nature, yet large enough to permit the amplification of magnetic fields. The magnetic Reynolds number  $R_M$  is defined as  $\frac{vl}{\eta}$  where  $v, l$ , and  $\eta$  are a typical speed, a typical length scale, and magnetic diffusivity, respectively. The Spitzer classical magnetic diffusivity  $\eta$  is given by  $10^{13}T^{-3/2}cm^2s^{-1}$ . Using typical numbers for the SNR case,  $T \approx 10^7 \sim 10^8K$ ,  $v \approx 10^8cm/s$ , and  $l \approx 0.1pc$ , we obtain a magnetic Reynolds number of about  $10^{24}$ . This number is much larger than the typical solar magnetic Reynolds number  $10^7$ , and vastly larger than what can be simulated directly. This result is not as discouraging as it seems, for two reasons. First, we have estimated  $R_M$  using the classical value for  $\eta$ , and this ignores anomalous diffusivities which are orders of magnitude larger in diffuse plasmas because, for a turbulent plasma, the collision time and corresponding electrical conductivity can often be much smaller than the Spitzer values (Priest 1982). Second, while although we are not treating the small scale magnetic fields correctly, we believe we are modeling the large scale fields correctly. This means that the radio luminosity which is sensitive to the small scale field, is underestimated, whereas the radio polarization which is determined by the large-scale field is accurately computed. Insofar as the radio luminosity is uncertain to within the normalizing factor in eq.(8), whereas we are primarily interested in understanding the polarization properties of young SNR, our simulations are still providing us some useful new results. We expect that the volume occupied by the dynamically important fields may increase in higher resolution 3D simulations. However, it is still uncertain if equipartition between turbulent energy and magnetic energy is obtained on the time scale of a real SNR. The equipartition may be achieved at least in small scales since the eddy-turnover time is shorter for small scale structures. Despite all

of numerical difficulties, we believe that our current calculation still serves a good basis for understanding global features such as *large scale structures of magnetic fields* which was one of our original motivation for this study.

## 5. Discussions and Conclusions

We defer a detailed comparison with observations to our forthcoming paper presenting the results of full 3D simulations of young SNR (Jun & Norman 1995). However, some useful comparisons can already be made on the basis of the 2D simulations. In Fig.11, the angle-averaged magnetic fields shows a maximum value about  $2 \times 10^{-5}G$  near the contact discontinuity. This is about one order of magnitude lower than the estimated value  $3 \times 10^{-4}G$  in Tycho's SNR (Strom and Duin 1973). As we discussed in Sec.4, this is very likely an effect of numerical resolution limiting the amplification of magnetic fields on small scales. In addition, it should be noted that the estimated strength of magnetic field in young SNR is only a rough value because the minimum energy requirement is used to obtain it. The condition for minimum energy requirements corresponds closely to the condition of equipartition of energies in the relativistic particles and the magnetic field (e.g. see Longair 1992). However, there is no physical justification for the equipartition. The information about a filling factor (the fraction of the volume occupied by radio emitting material) is an another uncertainty in the observation. Since our result of magnetic-field strength is much lower than the strength estimated by the equipartition assumption in young SNRs, the higher energy of relativistic electrons is required to account for the observed radio luminosity of young SNRs.

The surface brightness predicted from our simulation shows that main shells of radio and X-ray emission are close to each other but not exactly coincident. This result may explain the coincidence of the inner radio shell and X-ray emission in the main shell of Tycho's SNR. However neither our simulation nor observation show detailed correspondence between radio and X-ray features. This is explained in our model as a simple result of the nature of the strongly emitting regions in these two wavebands : the X-rays are emitted by the dense fingers of stellar ejecta, whereas the radio emission preferentially samples the strong magnetic field lines draped around the R-T fingers.

One of the most puzzling features in young SNRs is the bright rims in Tycho's SNR and the SNR of A.D. 1006 which our model does not explain. Dorfi (1990) has studied the cosmic-ray driven instability in young SNR, and has found that the region in the precursors of two shocks is unstable. However, this instability generally requires a dominant cosmic-ray pressure which is in doubt (Markiewicz et al. 1990; Drury et al. 1995). One can also ask why rims are not seen in all young SNRs if this instability is a generic feature of the shock in SNR. The detailed hydrodynamical simulation of this instability in multi-dimensions should be pursued. Another possible mechanism is the clumpy medium model(e.g. Dickel et al. 1989). Although we don't know have detailed information about the inhomogeneity in the ambient medium, it is worth studying the effect of the clumpy medium in general. This model has been investigated very recently with encouraging results (Jun 1995). The clumpy medium model is found to produce a thicker and clumpier mixing layer than a uniform medium model with a dominant radial component of magnetic fields.



We have carried out the first 2D nonlinear MHD simulations of a young supernova remnant propagating into a uniform density, uniformly magnetized medium. Our moving grid technique has allowed us to study the instability of the mixing layer between the stellar ejecta and the swept up ISM in both the Chevalier (2-shock self-similar) and non-self-similar regimes. Summarizing our main results, we find :

1. The R-T and K-H instabilities in the mixing layer amplify the existing magnetic fields locally by as much as a factor of 60 around dense fingers by the stretching and the compression of active fingers. Globally, the angle-averaged magnetic fields near the contact discontinuity increased to about  $2 \times 10^{-5}G$  from an ambient value of  $3.5 \times 10^{-6}G$ .
2. Equipartition between the turbulent energy density and magnetic energy density is not achieved globally. The magnetic energy density reaches only about 0.3 % of the turbulent energy density by the end of simulation. The amplified field becomes dynamically important locally around the active finger. However the magnitude of amplification is sensitive to numerical resolution.
3. The R-T instability model produces thick clumpy radio and X-ray (thermal bremsstrahlung) shells inside of the outer shock. The X-ray emission peaks inside of the radio emission but they are close each other. Our model shows that there is no detailed correspondence between substructure in the radio and X-ray emission.
4. The time history of luminosity reflects the dynamics of the remnant and the instability. Both the radio and X-ray (thermal bremsstrahlung) luminosities increase during the self-similar stage but then decrease as the remnant evolves beyond the

self-similar stage.

5. Our simulation produces comparable or dominant (at late stages) radial magnetic fields in the main radio shell. However, our model cannot account for radial magnetic fields adjacent to the outer shock front, which may require additional instabilities to generate.

We are grateful to Fausto Cattaneo, John Dickel, Tom Jones, and Bob Rosner for the useful discussion. We also thank Roger Chevalier for comments. A number of constructive comments by the referee, Steve Reynolds were particularly useful. The simulations were done on the Cray C90 at the Pittsburgh Supercomputing Center.

## References

- [1] Anderson, M., Rudnick, L., Leppik, P., Perley, R., & Braun, R. 1991, *ApJ*, 373, 146.
- [2] Ardavan, H. 1973, *ApJ*, 184, 435.
- [3] Band, D.L. & Liang, E.P. 1988, *ApJ*, 334, 266.
- [4] Cattaneo, F., Chiueh, T., & Hughes, D.W. 1990, *J. Fluids Mech.*, 219, 1.
- [5] Chandrasekhar, S. 1961, *Hydrodynamic and Hydromagnetic Stability*, Oxford University Press.
- [6] Chevalier, R.A. 1982, *ApJ*, 258, 790.
- [7] Chevalier, R.A., Blondin, J.M., & Emmering, R.T. 1992, *ApJ*, 392, 118.
- [8] Clarke, D.A. 1988, Ph.D. thesis, Univ. New Mexico.
- [9] Colgate, S.A. & McKee, C. 1969, *ApJ*, 157, 623.
- [10] Cowsik, R. & Sarkar, S. 1980, *MNRAS*, 191, 855.
- [11] Dickel, J.R., Eilek, J.A., & Jones, E.M. 1993, *ApJ*, 412, 648.
- [12] Dickel, J.R., van Breugel, W.J.M., & Strom, R.G. 1991, *AJ*, 101, 2151.

- [13] Dickel, J.R., Eilek, J.A., Jones, E.A., & Reynolds, S.P. 1989, *ApJS*, 70, 497.
- [14] Dickel, J.R., Sault, R., Arendt, R.G., Matsui, Y., & Korista, K.T. 1988, *ApJ*, 330, 254.
- [15] Drury, L.O'C., Völk, H. J., & Berezhko, E.G. *A&A*, accepted.
- [16] Dorfi, E.A. 1990, *A & A*, 234, 419.
- [17] Downs, G.S. & Thompson, A. R. 1972, *AJ*, 77, 120.
- [18] Evans, C.R. & Hawley, J. F. 1988, *ApJ*, 332, 659.
- [19] Gull, S.F. 1973, *MNRAS*, 161, 47.
- [20] Gull, S.F. 1975, *MNRAS*, 171, 263.
- [21] Hamilton, A.J.S., Sarazin, C.L., & Szymkowiak, A.E. 1986, *ApJ*, 300, 713.
- [22] Henbest, S. N. 1980, *MNRAS*, 190, 833.
- [23] Jones, E.M., Smith, B.W., & Straka, W.C. 1981, *ApJ*, 249, 185.
- [24] Jun, B.-I. 1995, Ph.D. thesis, Univ. Illinois.
- [25] Jun, B.-I. & Norman, M.L. 1995b, in preparation.
- [26] Jun, B.-I. & Norman, M.L. 1995c, in preparation.
- [27] Jun, B.-I., Norman, M.L., & Stone, J.M. 1995, *ApJ*, 453, 332.
- [28] Longair, M.S. 1992, *High Energy Astrophysics*, Cambridge University Press.
- [29] Lou, Y.Q. 1994, *ApJ*, 428, L21.
- [30] Markiewicz, W.J., Drury, L.O'C., & Völk, H.J. 1990, *A&A*, 236, 487.
- [31] Matsui, Y., Long, K.S., Dickel, J.R., & Greisen, E.W. 1984, *ApJ*, 287, 295.
- [32] McKee, C.F. 1974, *ApJ*, 188, 335.
- [33] Milne, D.K. 1987, *Aust. J. Phys.*, 40, 771.
- [34] Priest, E.R. 1982, *Solar Magnetohydrodynamics*, (Dordrecht: Reidel).
- [35] Reynolds, S.P. & Gilmore, D.M. 1986, *AJ*, 92, 1138.
- [36] Reynolds, S.P. & Ellison, D.C. 1992, *ApJ*, 399, L75.
- [37] Reynolds, S.P. & Gilmore, D.M. 1993, *AJ*, 106, 272.
- [38] Sharp, D.H. 1984, *Physica D*, 12, 3.
- [39] Shull, J.M. 1982, *ApJ*, 262, 308.

- [40] Stone, J.M. & Norman, M.L. 1992a, *ApJS*, 80, 753.
- [41] Stone, J.M. & Norman, M.L. 1992b, *ApJS*, 80, 791.
- [42] Strom, R.G. & Duin, R.M. 1973, *A&A*, 25, 351.
- [43] Tan, S.M. & Gull, S.F. 1985, *MNRAS*, 216, 949.
- [44] Vainstein, S.I. & Rosner, R. 1991, *ApJ*, 376, 199.
- [45] Youngs, D.L. 1984, *Physica D*, 12, 32.
- [46] Youngs, D.L. 1991, *Phys. Fluids A*, 3, 1312.

## 6. Figure Captions

Figure 1. A schematic representation of a typical young SNR in our computational space.

Figure 2. One dimensional result of the evolution of SNR at 100 yrs.  $\log(\text{density})$  is the logarithm of gas density,  $v_1$  is the radial velocity,  $B_2$  is the tangential component of magnetic field, and  $p$  is the gas pressure.  $\mu = 0.23$ .

Figure 3. One dimensional result of the evolution of SNR at 300 yrs.  $\mu = 1.6$ .

Figure 4. One dimensional result of the evolution of SNR at 500 yrs.  $\mu = 3.94$ .

Figure 5. The comparison of deceleration constant between our numerical simulation and Chevalier's self-similar solution. The velocity is taken at the contact discontinuity.  $\log(g)$  is the logarithm of deceleration constant and  $\log(\text{velocity})$  is the logarithm of the velocity at the contact discontinuity.

Figure 6. The grey scale images of the gas density (left images) and magnetic pressure (right images) at 500,400,300,200,100 years from top to bottom. The black color corresponds to the maximum value in the data.

Figure 7. The grey scale image of the gas density, the magnitude of magnetic field, the vorticity, and the current density in the shell region at 500 years from top to bottom. The black color corresponds to the maximum value in the data. In the vorticity and current density images, white (black) represent negative (positive) values, respectively.

Figure 8. The evolution of a peculiar magnetic energy density and a turbulent energy density.  $E_{mag1}$  is the radial component of the peculiar magnetic energy density,  $E_{mag2}$  is the circumferential component of the peculiar magnetic energy,  $E_{mag}$  is the total peculiar magnetic energy density,  $E_{tur1}$  is the radial component of the turbulent energy density,  $E_{tur2}$  is the circumferential component of the turbulent energy density, and  $E_{tur}$  is the total turbulent energy density.

Figure 9. The evolution of the thicknesses of a magnetic shell and an intershock region. The thickness is normalized by the radius of the forward shock front.

Figure 10. Energy spectra at 400 years.  $\log(\text{energy})$  is the logarithm of each energy at the region of the instability. In legend, kinetic energy is the turbulent energy density while magnetic energy is the peculiar magnetic energy density.

Figure 11. Angular average of the magnitude of the magnetic field at 500 years. The first plot is the tangential component of a magnetic field from a 1D simulation, the second plot is the angular average of the magnitude of a magnetic field from the 2D simulation, the third plot is the angular average of the magnitude of radial component of a magnetic field, and the fourth plot shows the angular average of the magnitude of tangential component of a magnetic field.

Figure 12. The spectra of peculiar magnetic energy component at 400 years(top graph) and 500 years(bottom graph).

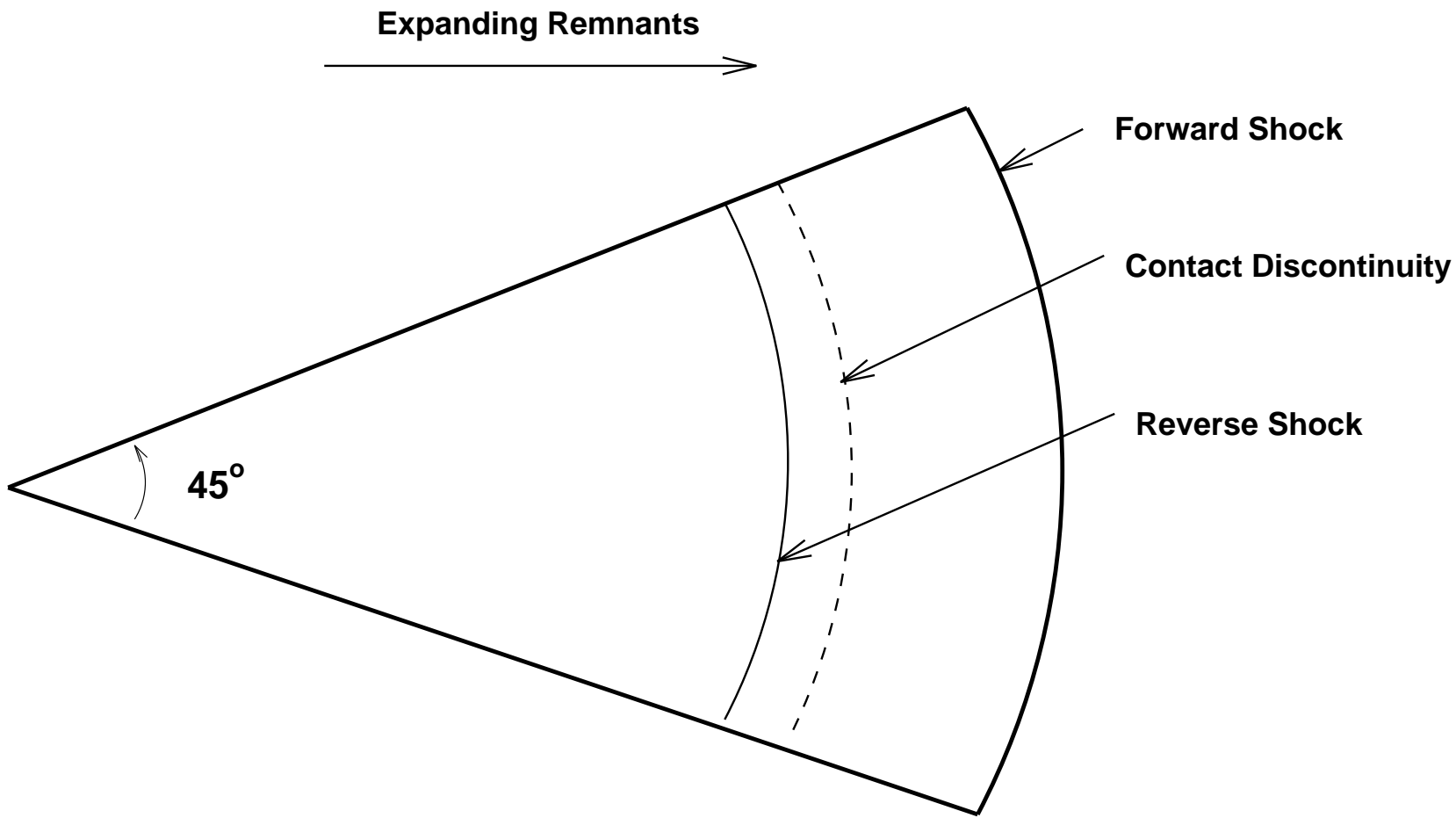
Figure 13. Grey scale images of radio (left) and X-ray (right) emission at 500 yrs.

Figure 14. Surface brightness profiles of radio and X-ray. The radius is normalized

by the radius of a forward shock. The units of surface brightness are arbitrary. Each plot corresponds to the surface brightness at 100, 200, 300, 400, and 500 years from top to bottom.

Figure 15. (a) Time history of radio luminosity. (b) Time history of X-ray luminosity. In legend, subscripts shell and shock represent the contribution from the main shell of the instability region and the contribution from the forward shock region, respectively.

Figure 16. The histogram of radio luminosity distribution at  $t=400$  years. Top histogram is the luminosity distribution from entire region while bottom histogram shows the luminosity from peculiar magnetic fields. The peculiar magnetic fields are obtained by subtracting magnetic fields from angular averaged magnetic fields. The vertical axis represents the partial luminosity divided by the total radio luminosity.

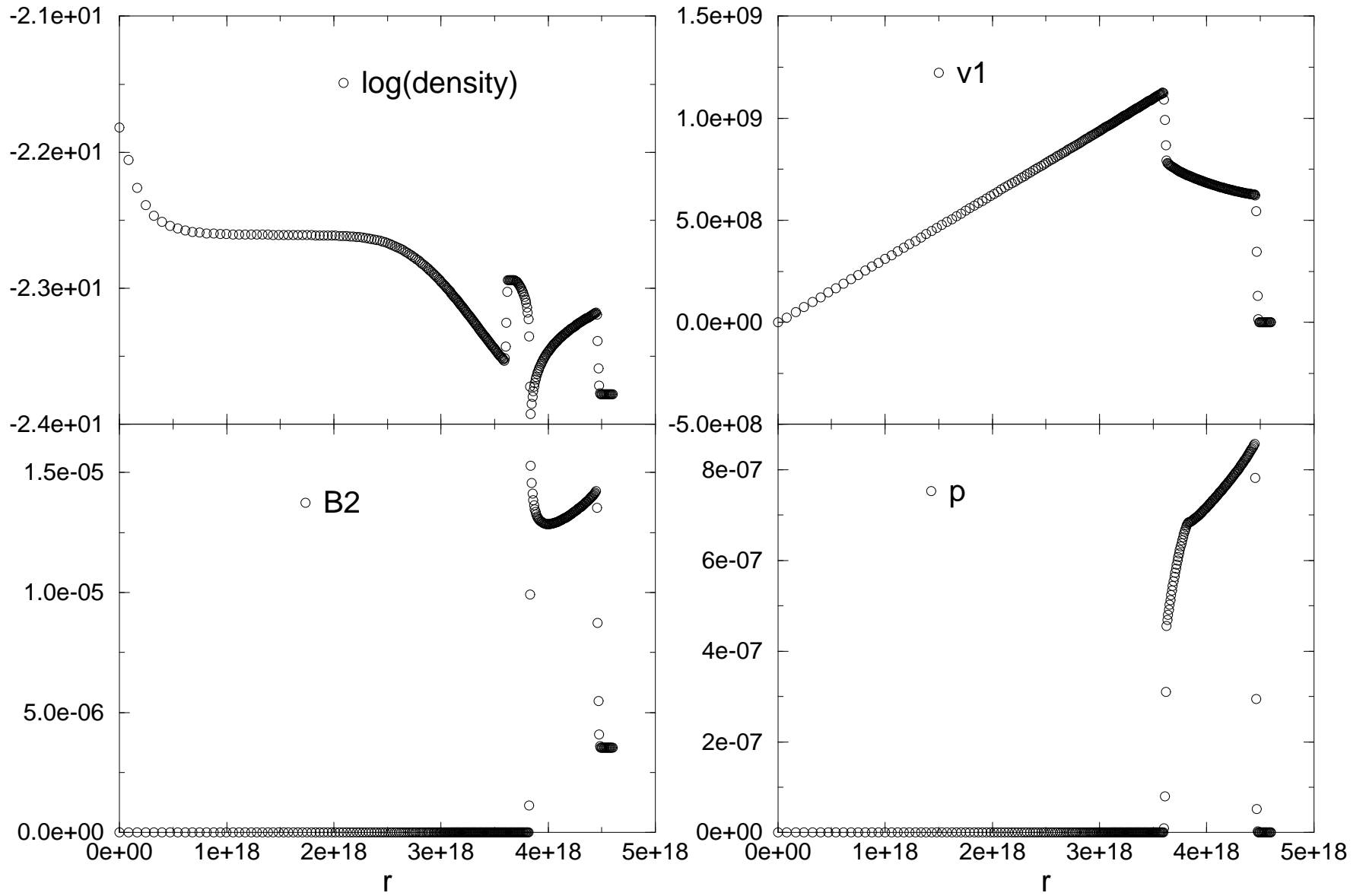


Coarse Ratioed Zones

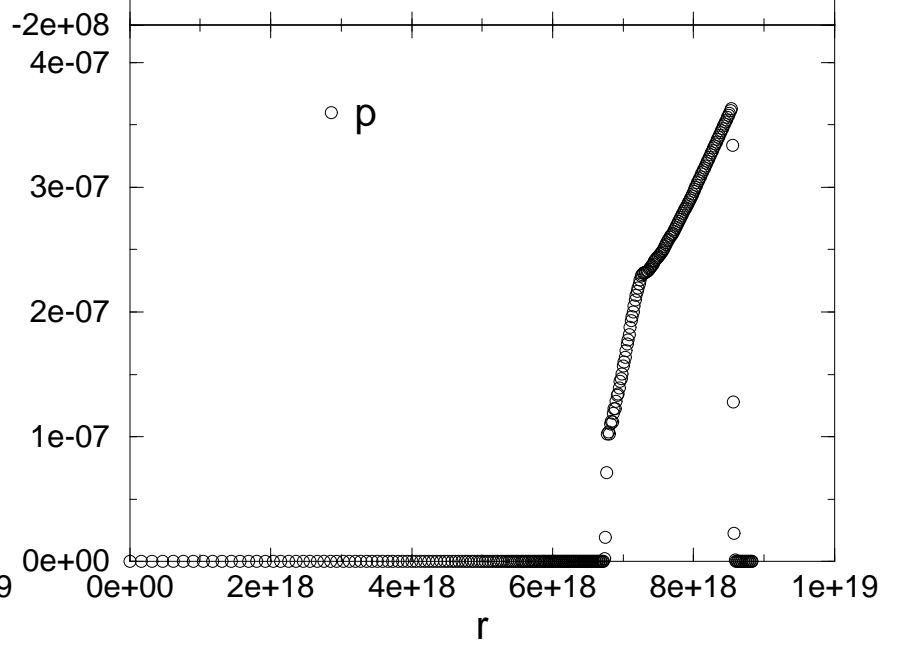
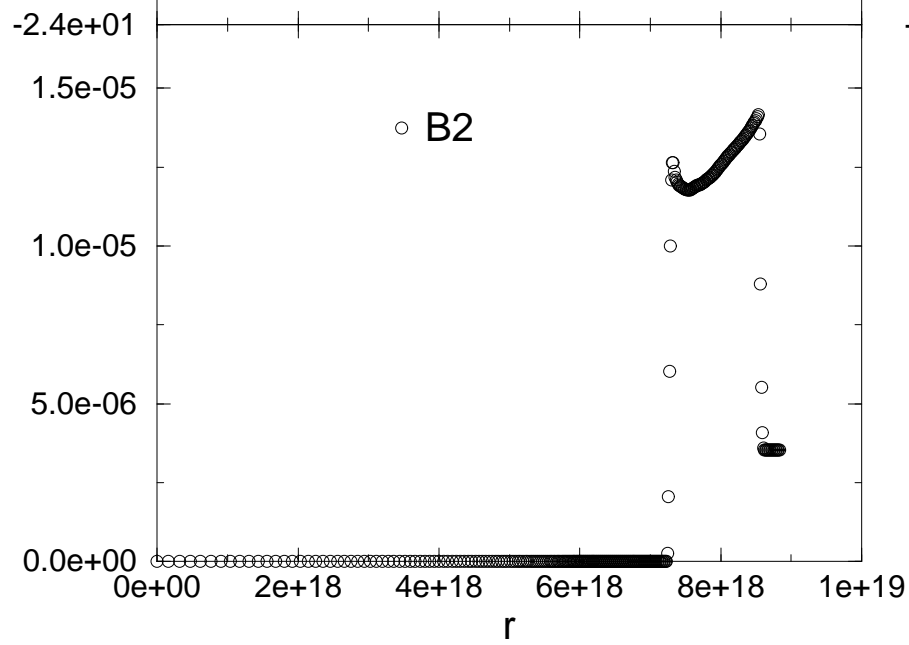
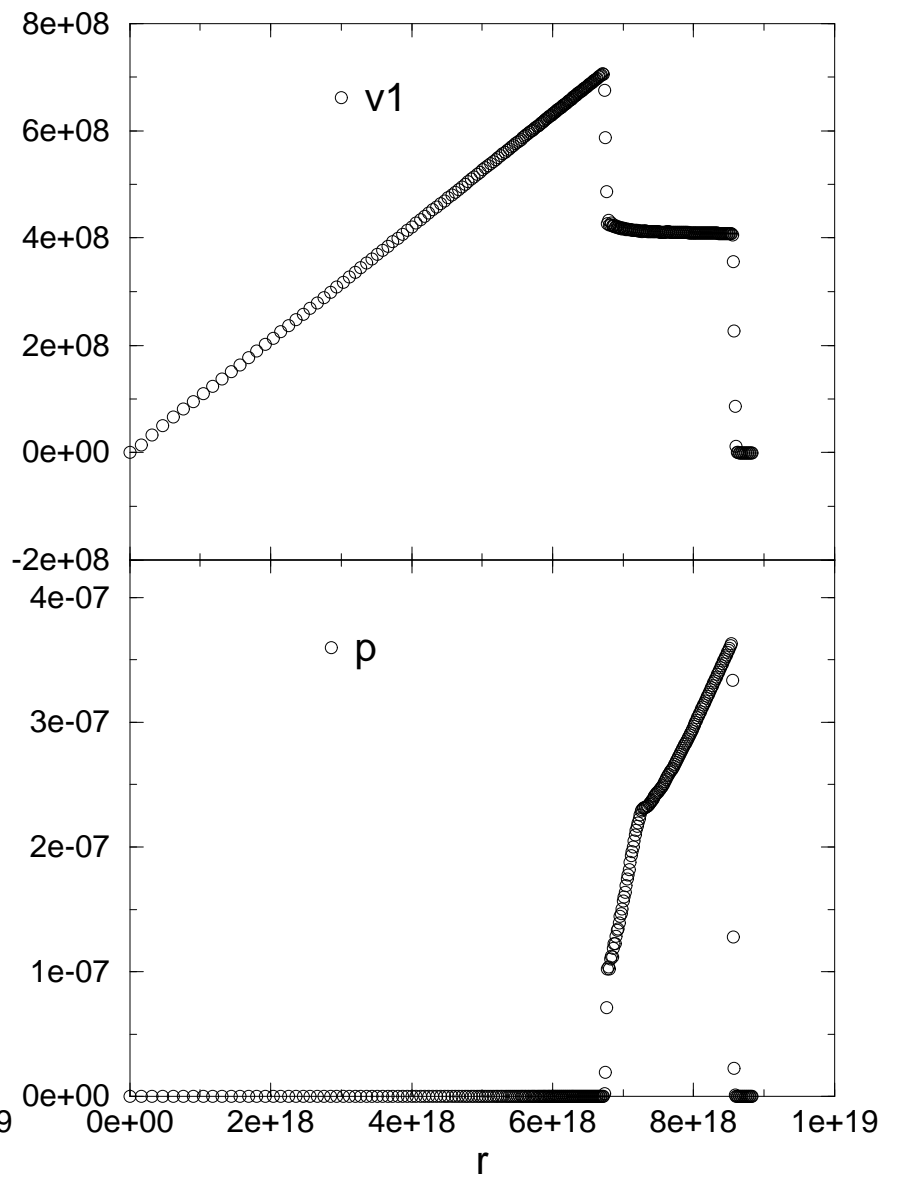
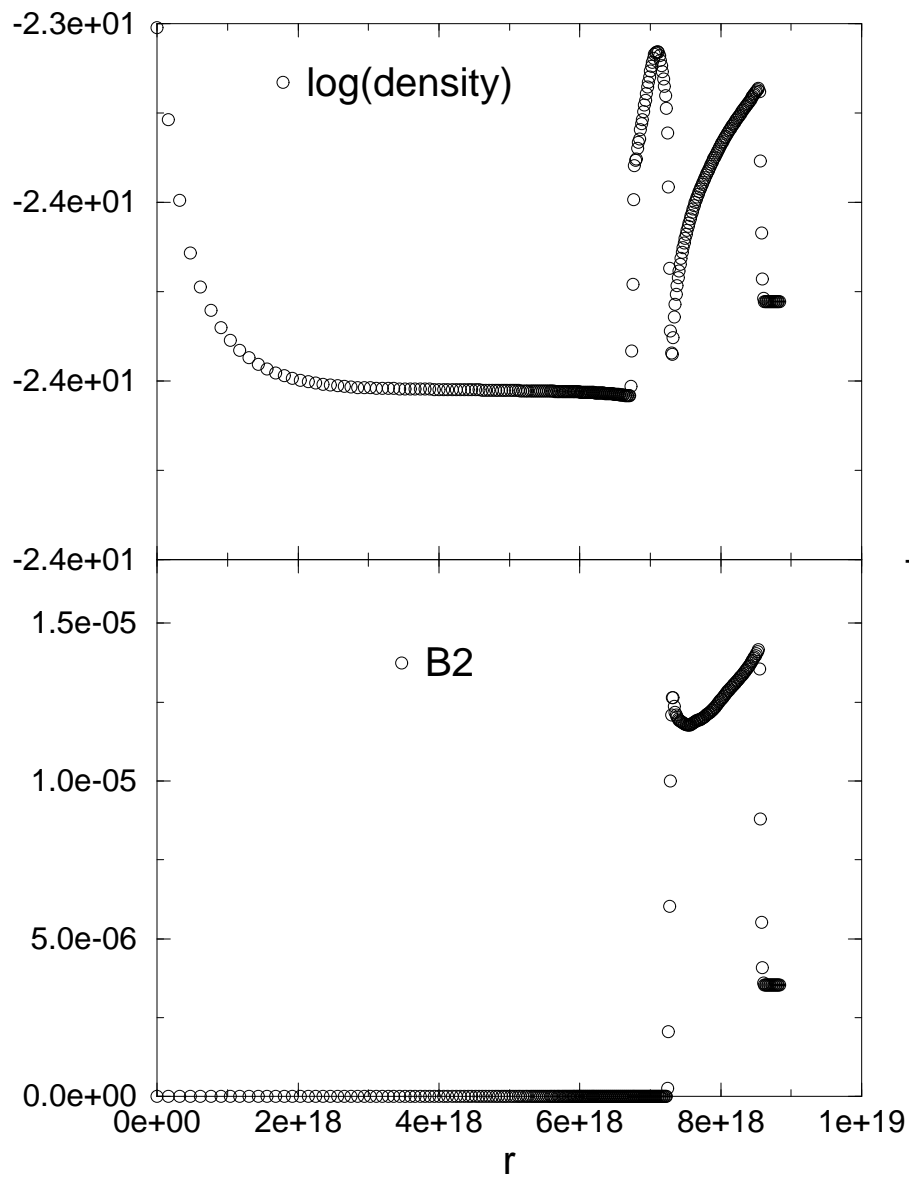
Fine Uniform Zones



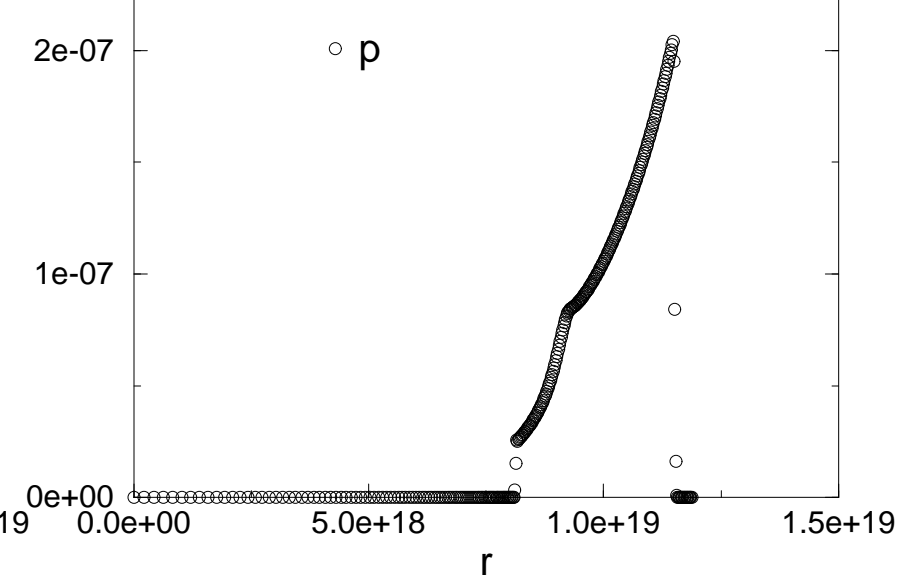
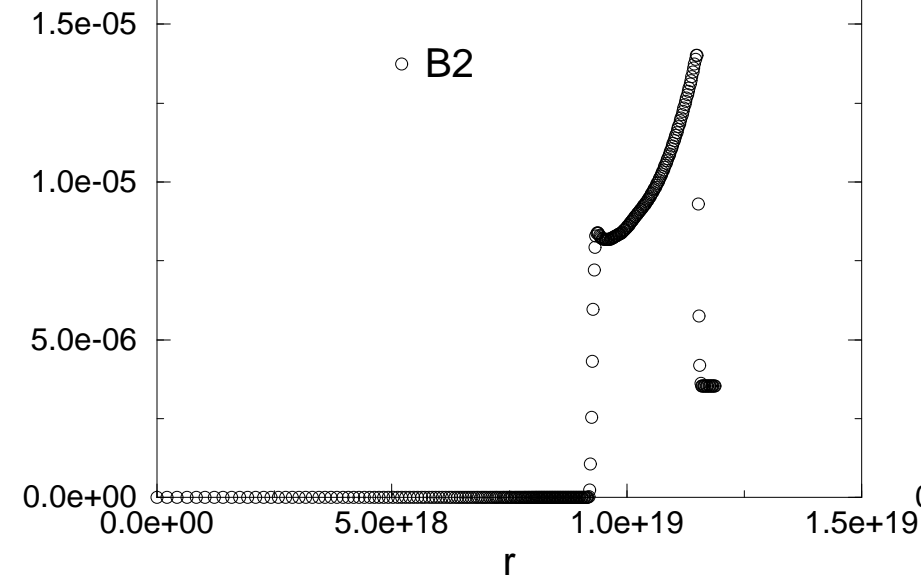
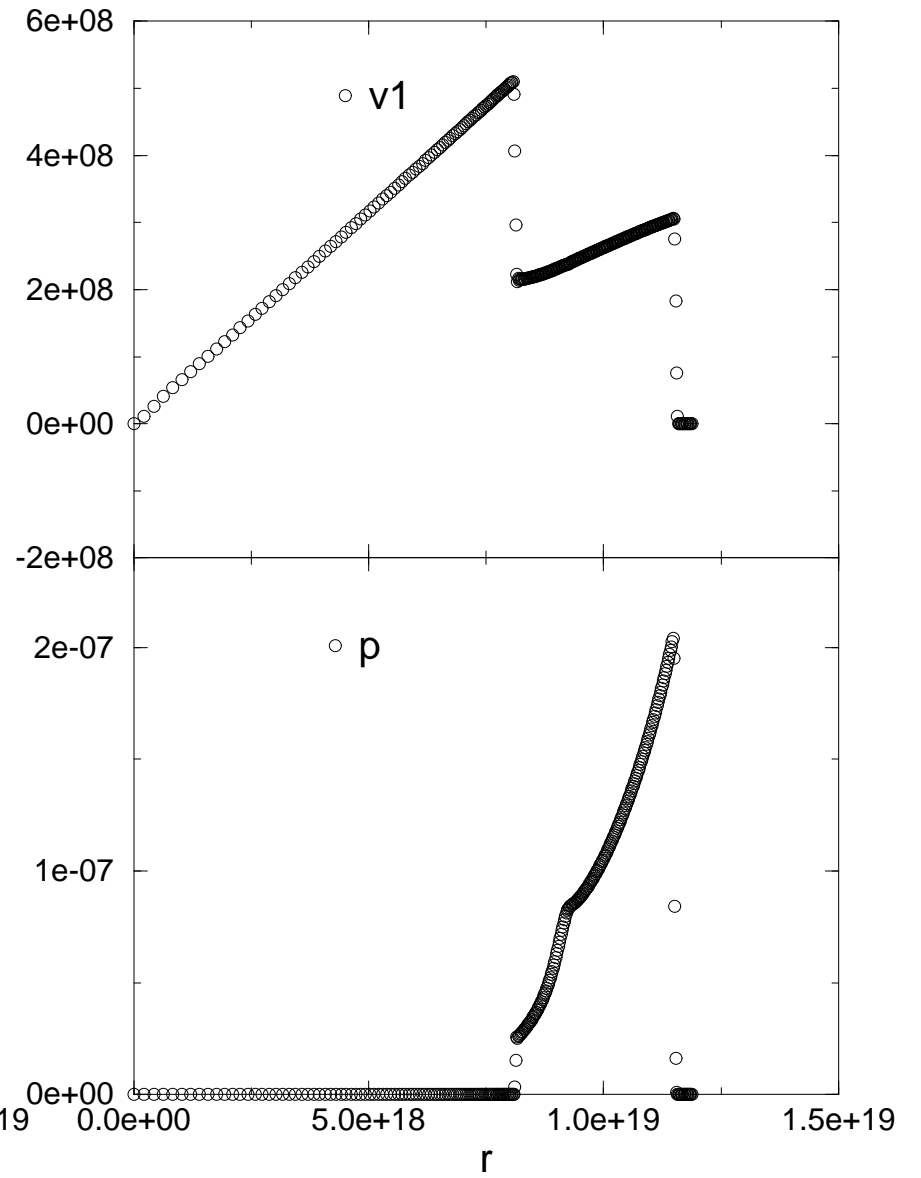
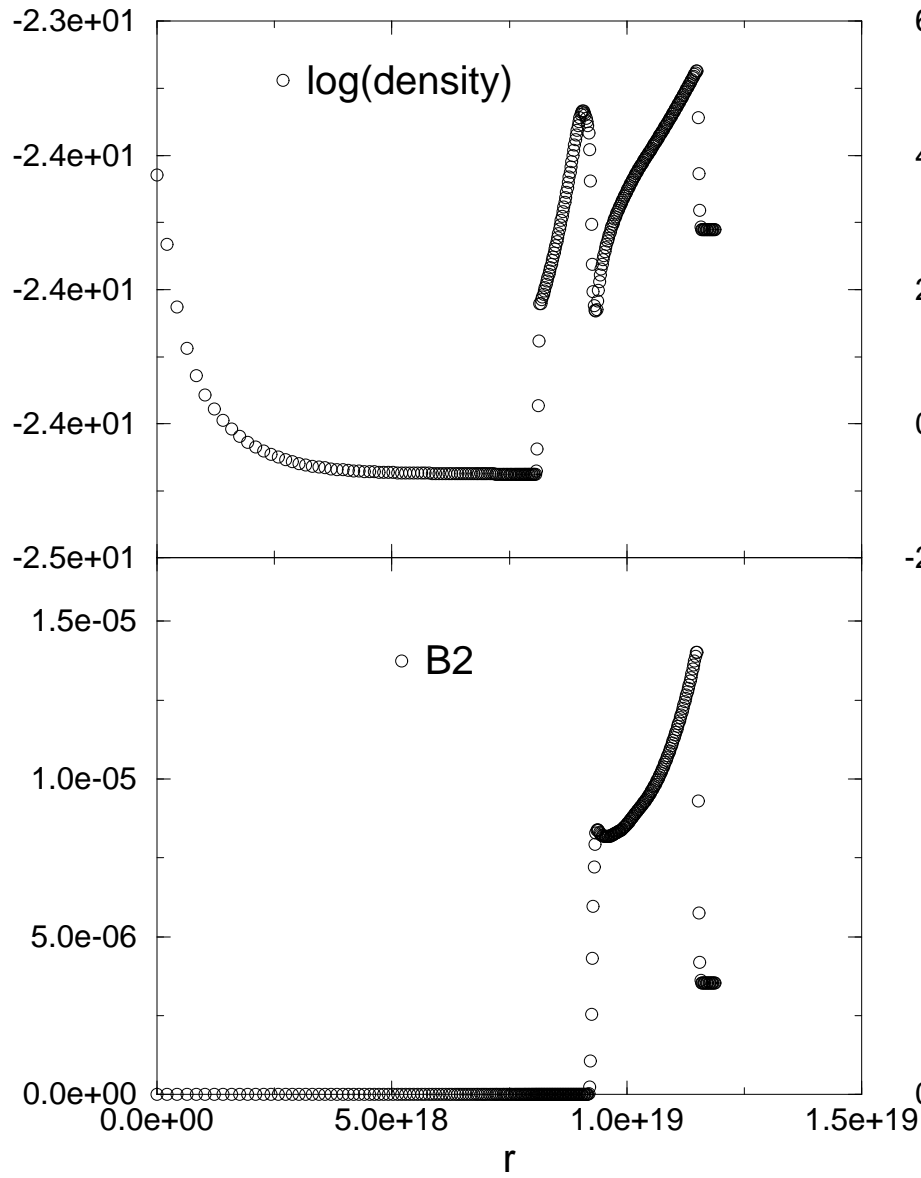
$t = 100 \text{ years}, \mu = 0.23$

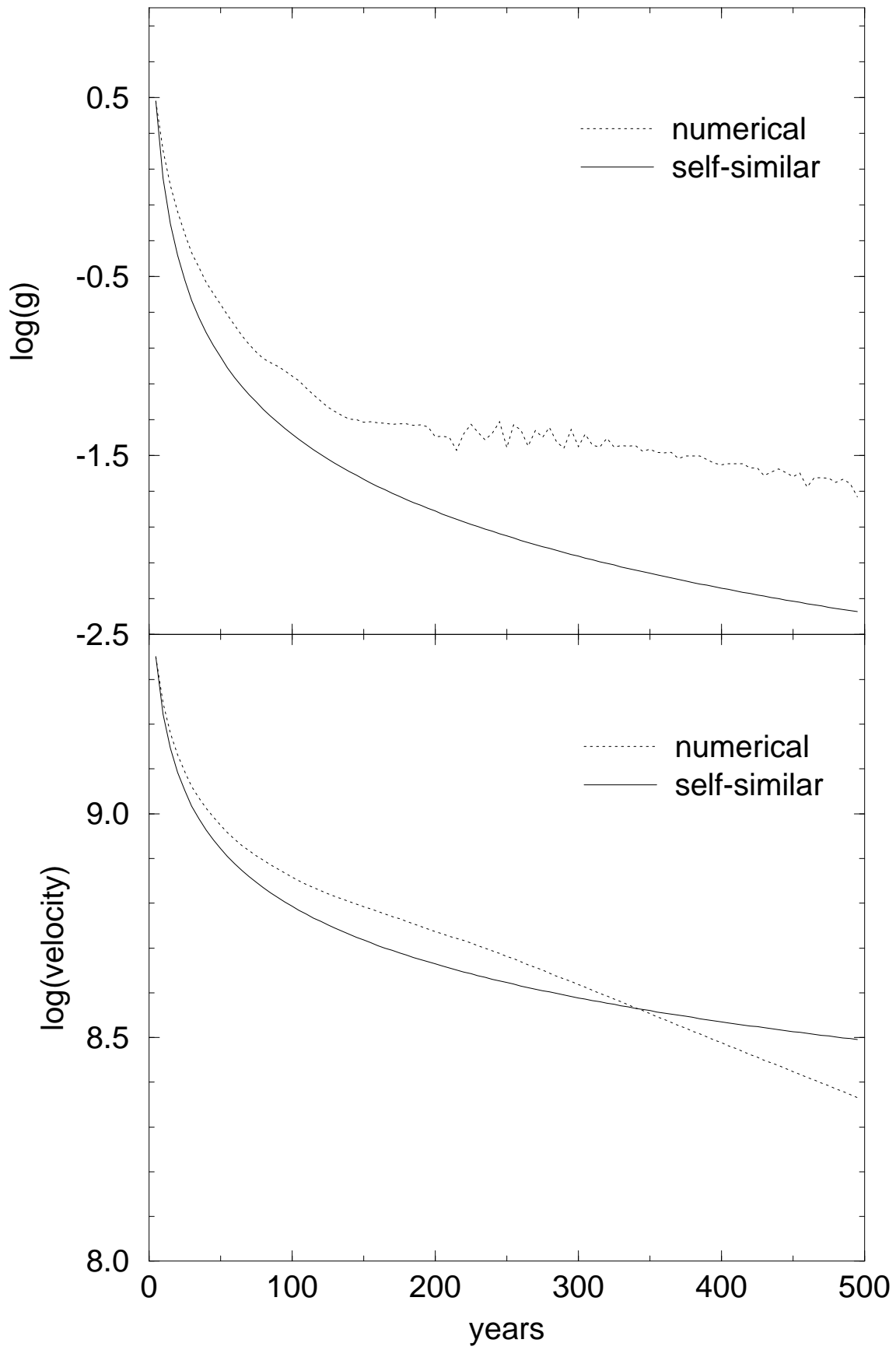


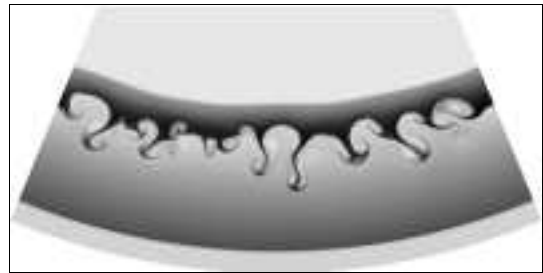
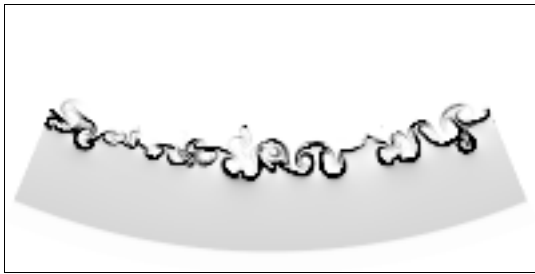
t = 300 years,  $\mu = 1.6$



$t = 500 \text{ years}, \mu = 3.94$





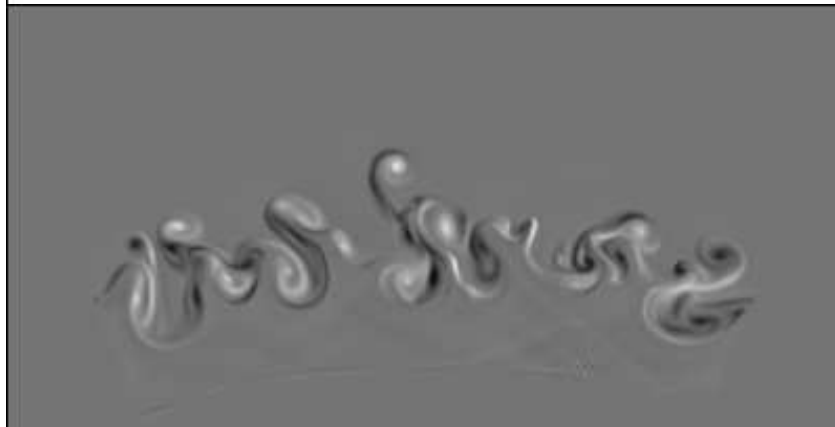




**density**



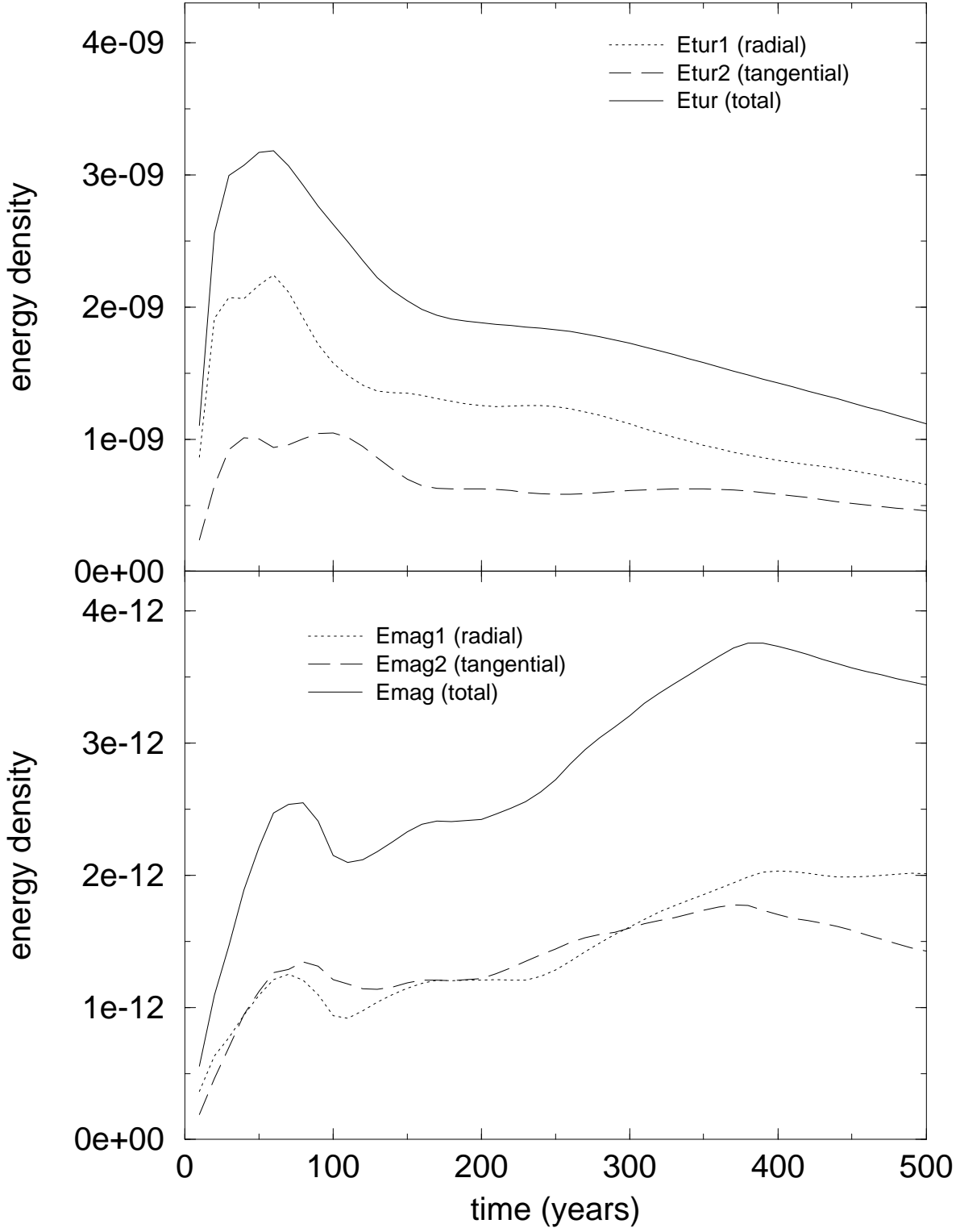
**magnetic  
field**

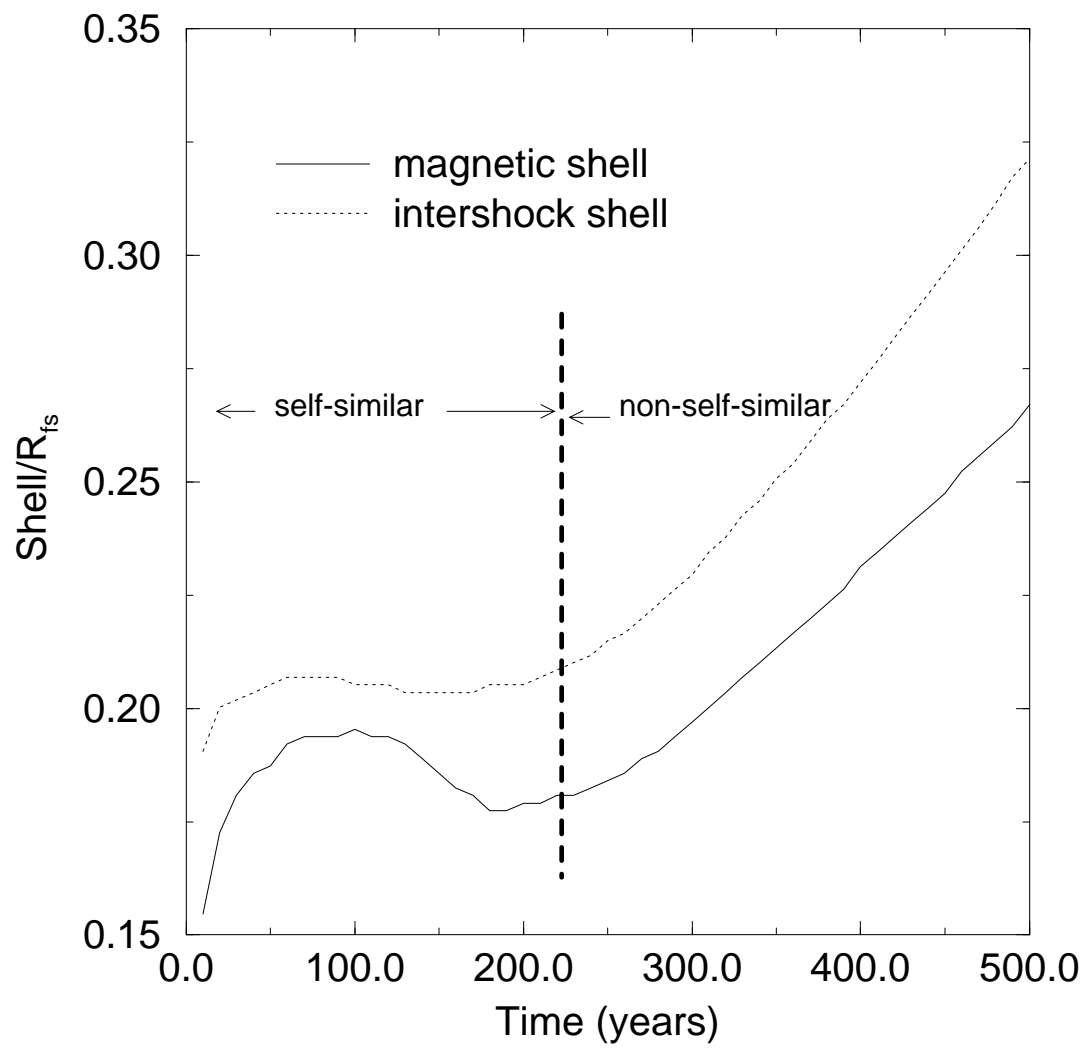


**vorticity**



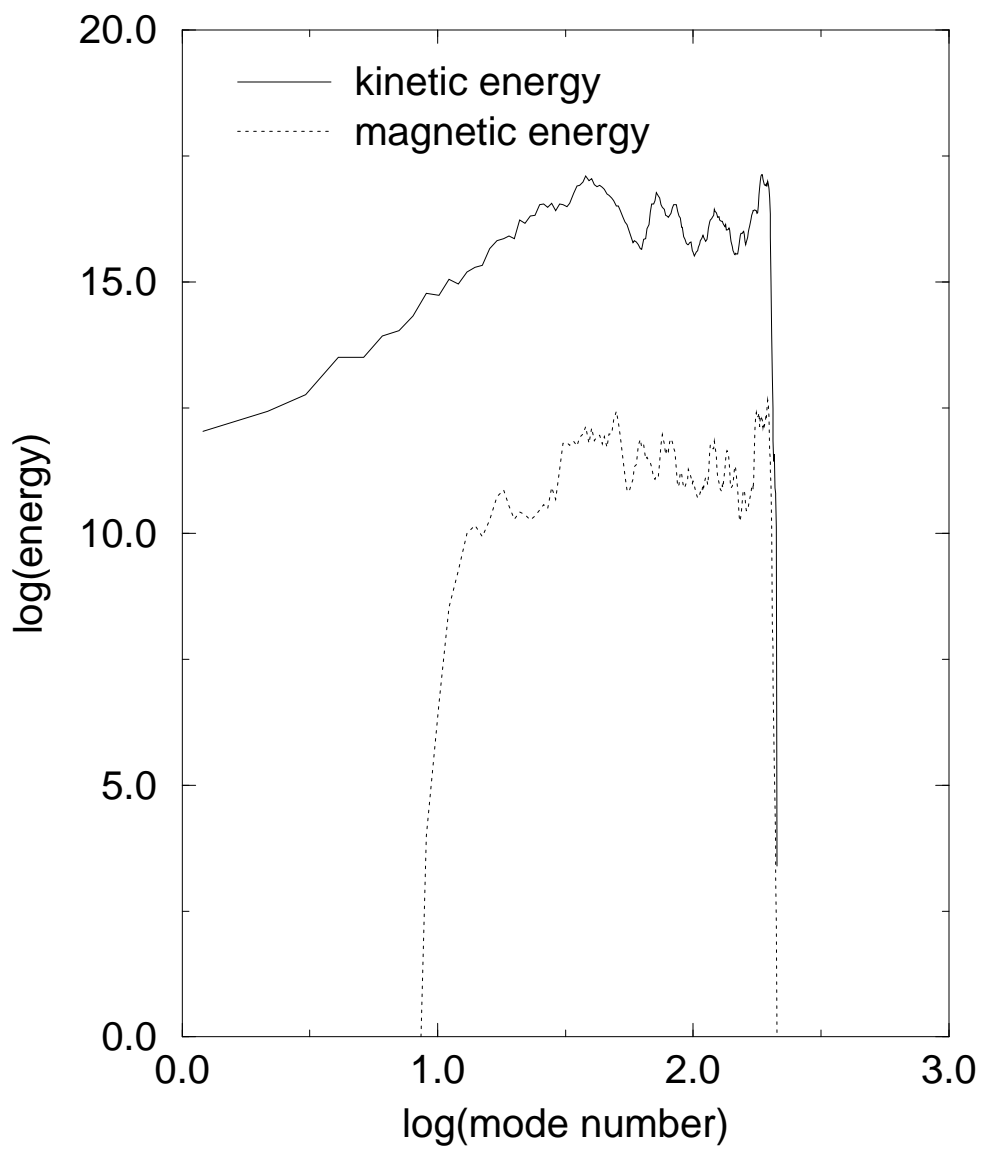
**current  
density**

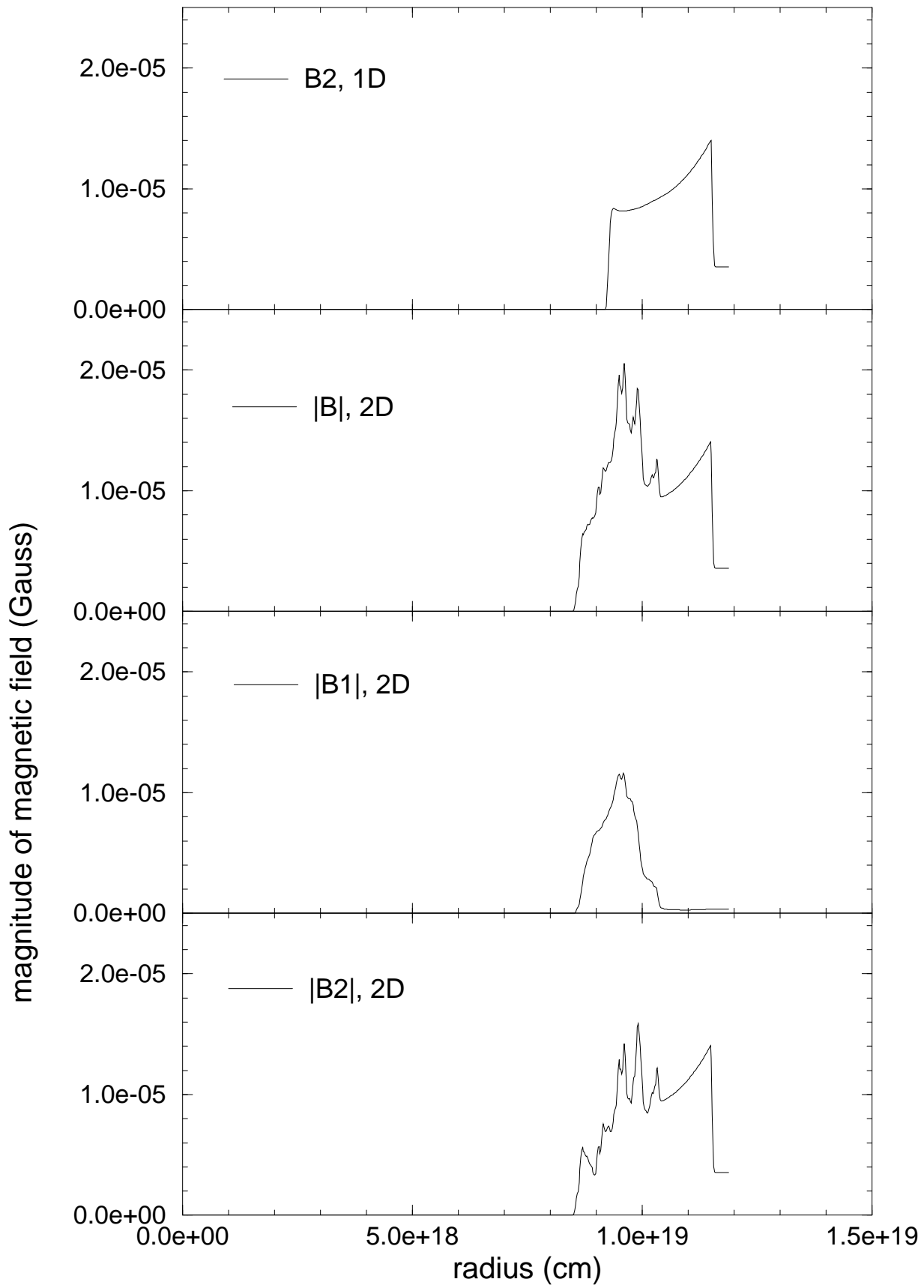


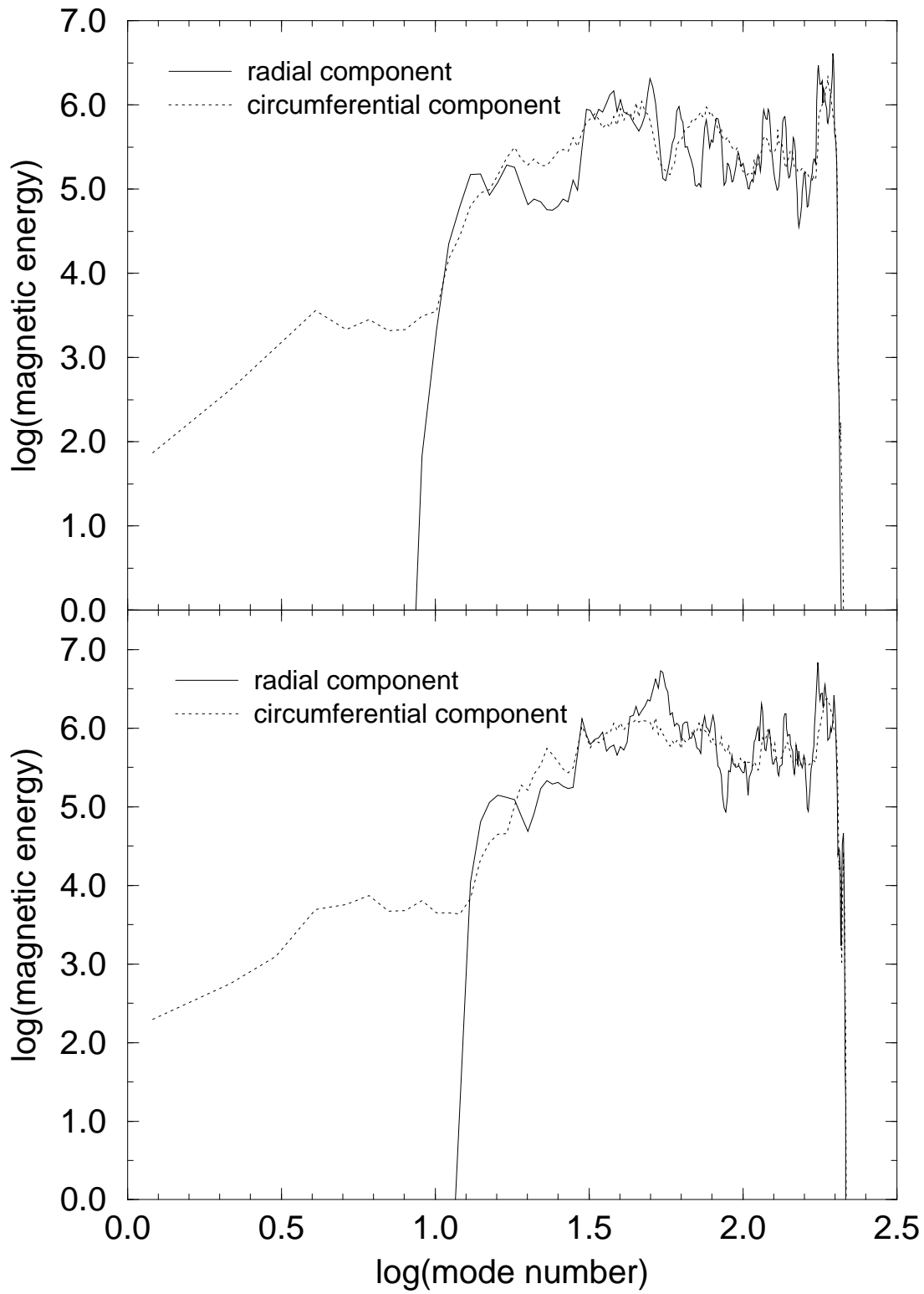


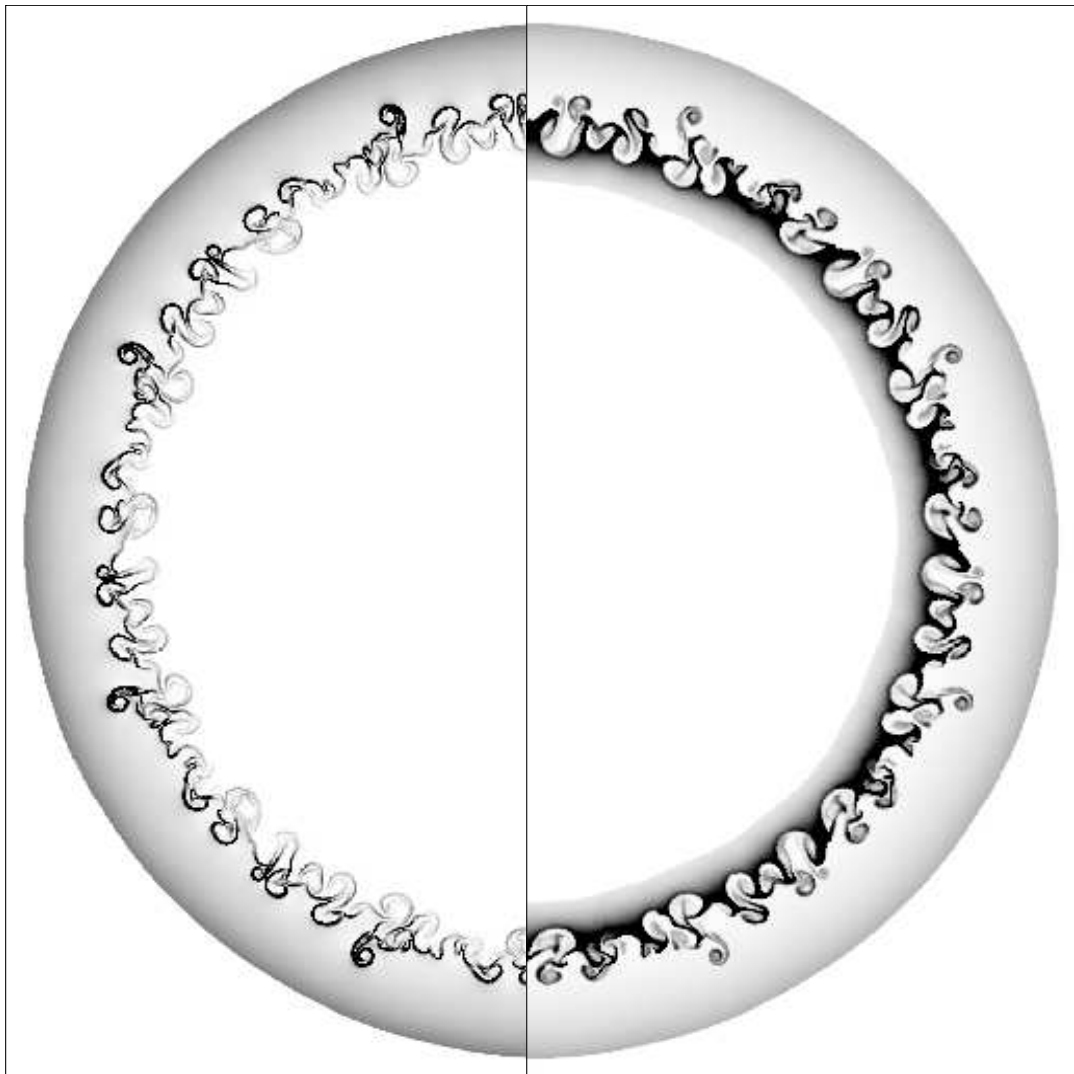


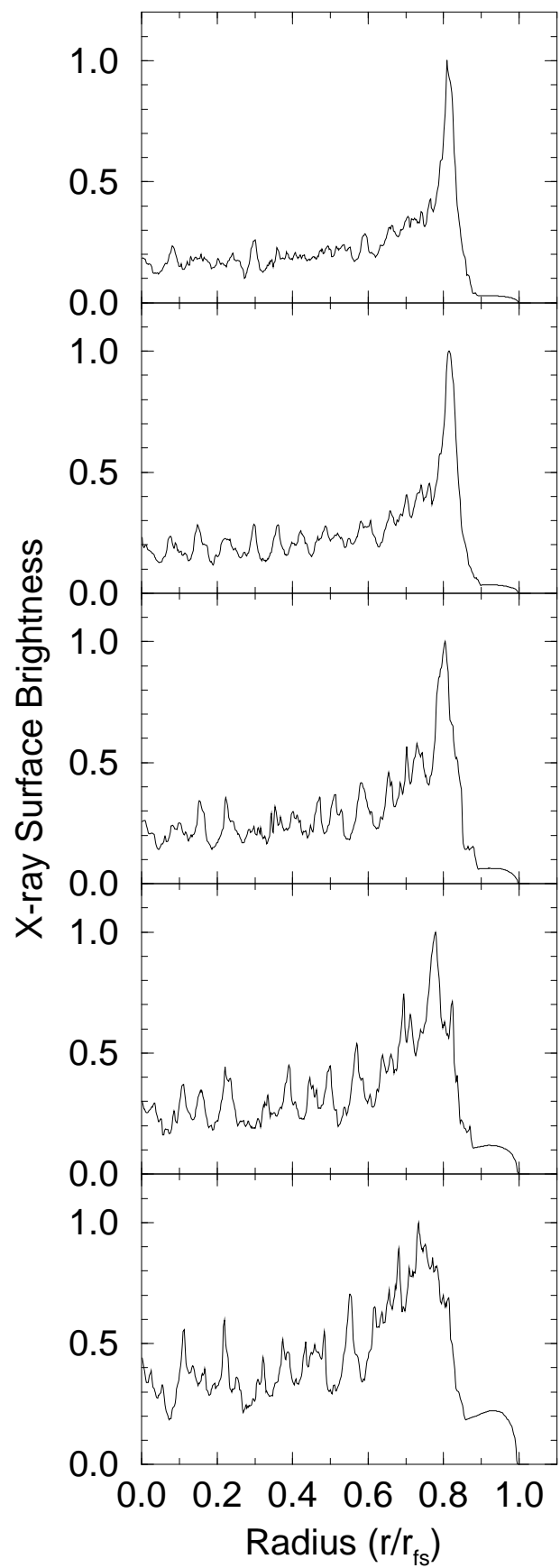
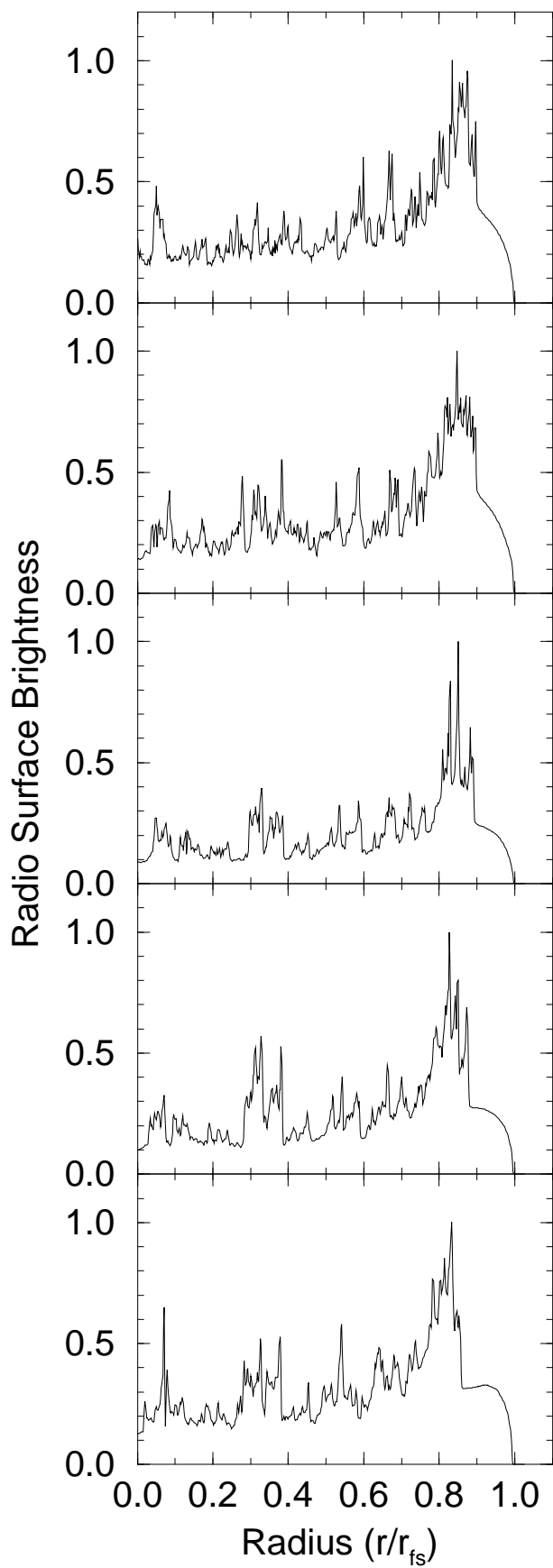
SNR at 400 years

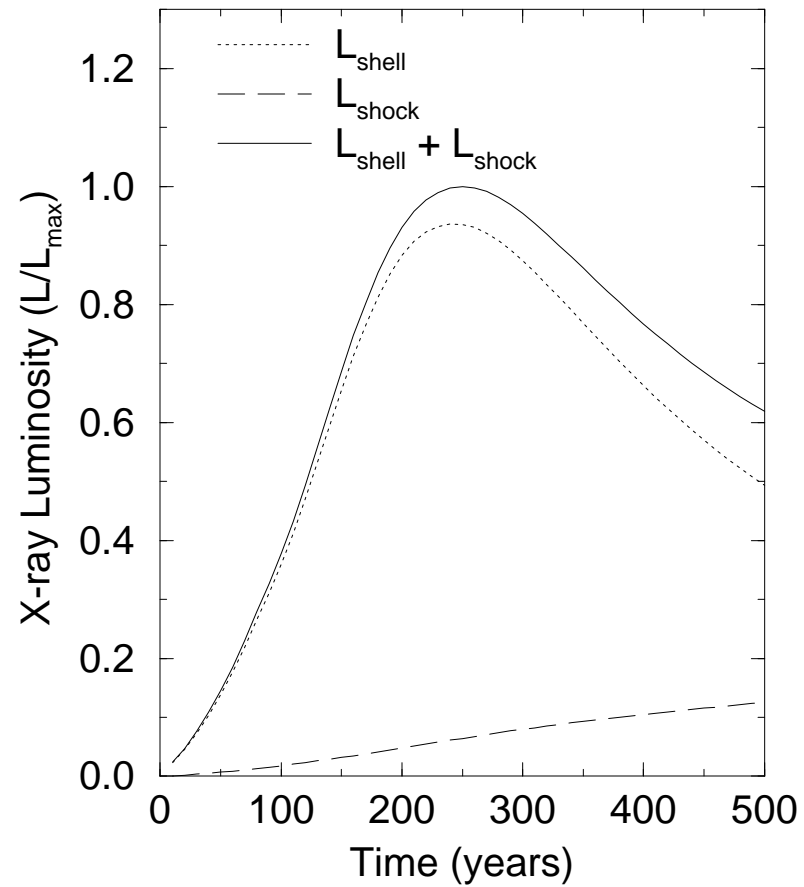
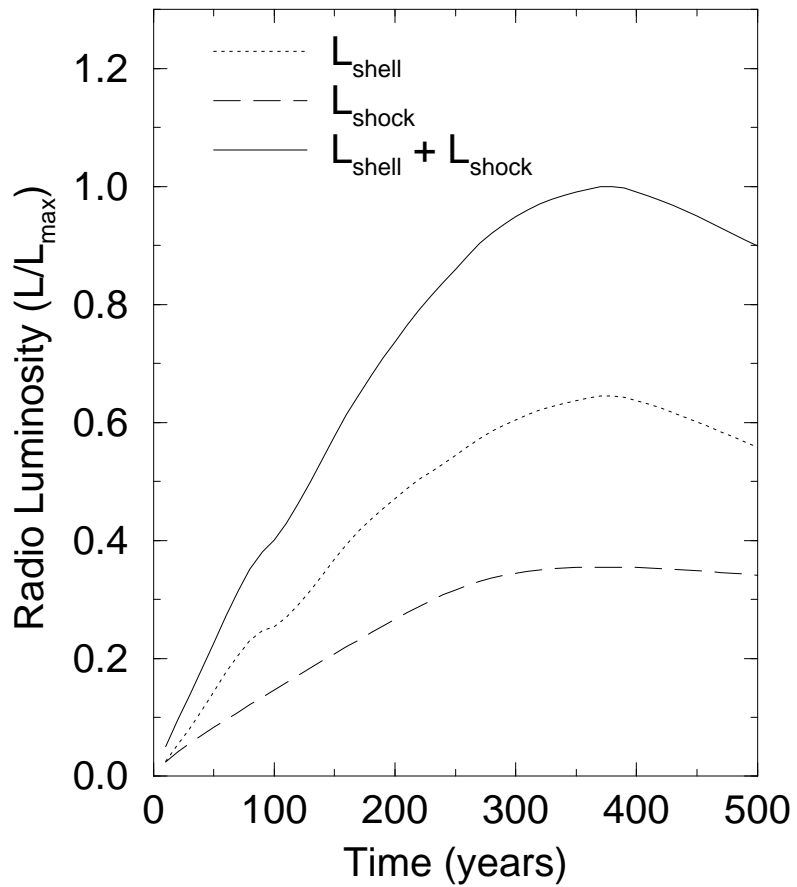




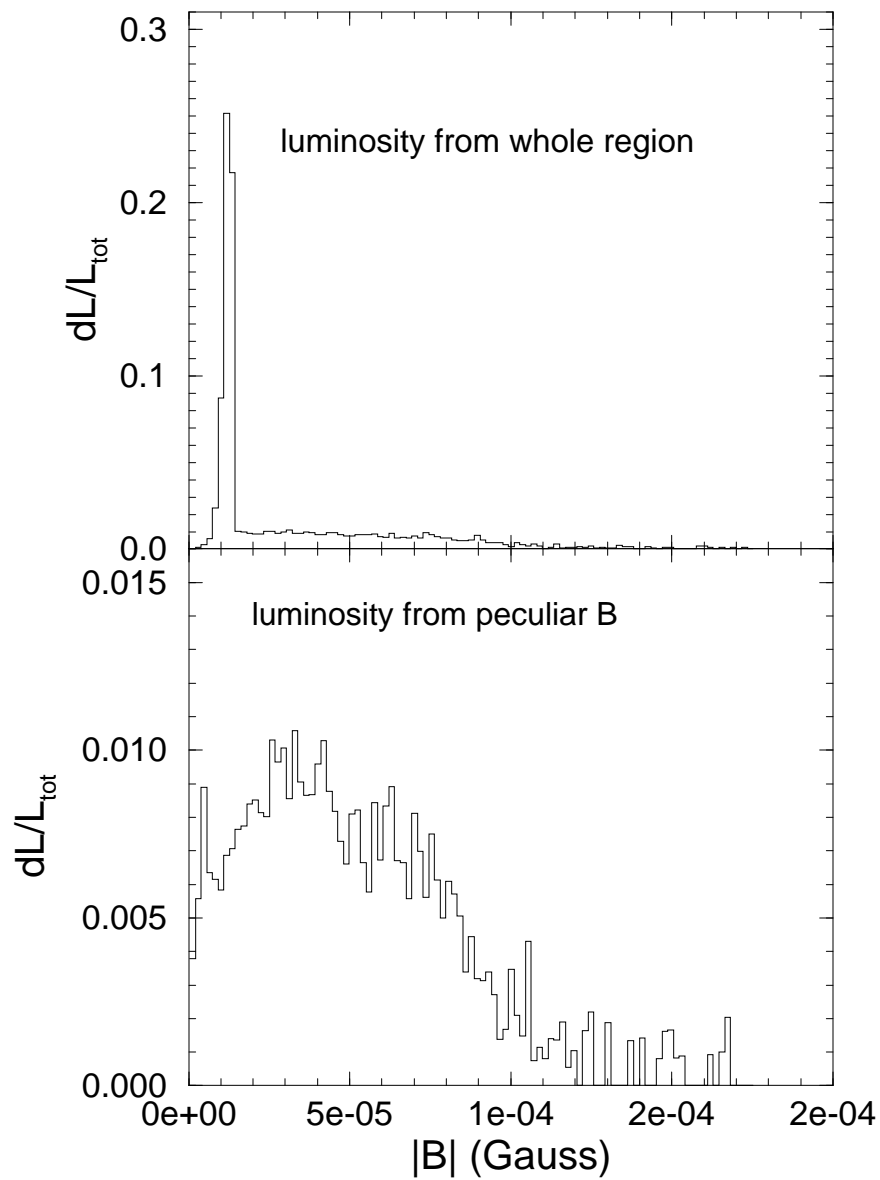








(a) Resolution : 300x400



(b) Resolution : 180x200

